Supporting Information

Electronically-Coupled Redox Centers in Trimetallic Cobalt Complexes

*Jeremy A. Intrator, Nicholas M. Orchanian, Andrew J. Clough, Ralf Haiges, and Smaranda C. Marinescu**

Department of Chemistry, University of Southern California, Los Angeles, CA, 900089, USA

E-mail: smarines@usc.edu

General

All manipulations of air and moisture sensitive materials were conducted under a nitrogen atmosphere in a Vacuum Atmospheres drybox or on a dual manifold Schlenk line. The glassware was oven-dried prior to use. All solvents were degassed with nitrogen and passed through activated alumina columns and stored over 4Å Linde-type molecular sieves. All the chemical reagents were purchased from commercial vendors and used without further purification. Ligands triphenylene-2,3,6,7,10,11-hexathiol (THT) and benzenehexathiolate (BHT) were prepared according to the reported procedures.[1,2]

Physical Methods.

NMR Spectroscopy

Proton NMR spectra were acquired at room temperature using Varian (Mercury 400 2-Channel, VNMRS-500 2-Channel, VNMRS-600 3-Channel, and 400-MR 2-Channel) spectrometers and referenced to the residual ^{1}H resonances of the deuterated solvent (^{1}H: DMSO, δ 2.50) and are reported as parts per million (ppm) relative to tetramethylsilane. ^{31}P resonances are reported as parts per million relative to 85% H_3PO_4, which is set as 0 ppm. ^{19}F resonances are reported as parts per million relative to fluorobenzene, which is set as –112.7 ppm.[3]

Elemental analyses

Elemental analyses were performed by Complete Analysis Laboratories, Inc., Parsippany, New Jersey or Robertson Microlit Laboratories, New Jersey.

UV-Vis NIR spectroscopy

Spectra were obtained using a Lambda 950 UV/Vis/NIR Spectrophotometer. Samples were analyzed in transmittance mode with a 1 cm quartz cuvette, and the spectrum measured for a blank acetonitrile sample was subtracted as background.

Single-crystal X-ray Diffraction

Diffraction data were collected on a Bruker SMART APEX DUO 3-circle platform diffractometer, equipped with an APEX II CCD, using Mo Kα radiation (TRIUMPH curved-crystal monochromator) from a fine-focus tube. The diffractometer was equipped with an Oxford Cryosystems Cryostream 700 apparatus for low-temperature data collection. The frames were integrated using the SAINT algorithm to give the hkl files corrected for Lp/decay. The absorption correction was performed using the SADABS program. The structures were solved by intrinsic phasing and refined on F2 using the Bruker SHELXTL Software Package and ShelXle. All non-hydrogen atoms were refined anisotropically.

Calculation of angular structural parameter τ

Calculation of the angular structural parameter, τ, was performed according to established protocol (Eq S1).[4] In Eq. S1, β and α are the two largest angles of the coordination center, where β > α. When τ approximates 0 this corresponds to the metal complex displaying a square pyramidal geometry, whereas when τ approximated 1, this corresponds to a trigonal bipyramidal geometry.

$$\tau = \frac{\beta - \alpha}{60}$$ **Equation S1**

X-ray Photoelectron Spectroscopy

XPS data were collected using a Kratos AXIS Ultra instrument. The monochromatic X-ray source was the Al K α line at 1486.6 eV. Low-resolution survey spectra were acquired between binding energies of 1–1200 eV. Higher-resolution detailed scans, with a resolution of ~0.1 eV, were collected on individual XPS lines of interest at a pass energy of 20. The sample chamber was maintained at $< 2 \times 10^{-8}$ Torr. The XPS data were analyzed using the CasaXPS software.

Electrochemistry

Cyclic and Differential Pulse Voltammetry (CV, DPV)

CV and DPV electrochemistry experiments were carried out using a Pine potentiostat. The experiments were performed in a single compartment electrochemical cell under a nitrogen atmosphere using a 3 mm diameter glassy carbon electrode as the working electrode, a platinum wire as auxiliary electrode and a silver wire as the reference electrode. All experiments in this paper were referenced relative to ferrocene (Fc) with the $Fe^{3+/2+}$ couple at 0.0 V, and all CVs were first scanned cathodically and subsequently returned anodically. All electrochemical experiments were performed in acetonitrile (MeCN), dichloromethane (DCM), or dimethylformamide (DMF) with 0.5 mM analyte concentration and 0.1 M tetrabutylammonium hexafluorophosphate as the supporting electrolyte. Ohmic drop was compensated using the

positive feedback compensation implemented in the instrument. All electrochemical experiments were performed with iR compensation using the current interrupt (RUCI) method in AfterMath.

Spectroelectrochemistry

Vis-NIR spectroelectrochemistry was carried out using an OTTLE cells equipped with a Pt minigrid auxiliary electrode, an Ag microwire pseudoreference electrode, a Pt minigrid working electrode and CaF2 windows.[5] Spectra were obtained using a Lambda 950 UV/Vis/NIR Spectrophotometer. A dichloromethane (DCM) solution of 2.5 M (TBA)(PF_6) was used to better solvate the produced reduced species and to avoid excess migration of reduced species to the auxillary electrode. Potentials were applied using a PalmSens EMStat3+. Electrolysis was performed at 25 mV increments and monitored via Vis-NIR. Starting potentials were chosen where no change in absorbance was observed for the initial isovalent species, and end points were achieved where no change in absorbance was observed. Equilibrium was attained via electrolysis for several minutes and verified using Vis-NIR. Reversibility was verified by reversing the electrolysis and ensuring that the spectrum of the starting material could be regenerated. The molar extinction coefficients for the MV species were obtained from the initial concentration of the parent isovalent complex, absorbance of the MV species, and pathlength of the OTTLE cell. Theoretical IVCT band width at half height ($\Delta v^0_{1/2}$) was obtained using the following equation[6]:

$$\Delta v^0_{\frac{1}{2}} = [16RTln2(v_{max})]^{1/2} \qquad \textbf{Equation S2}$$

where R is the ideal gas constant, T is the temperature in K, and ν_{max} is the energy at the max peak height of the IVCT band.

Computational Methods

Density Functional Theory (DFT) and Time Dependent DFT (TD-DFT)

All calculations were run using the Q-CHEM program package.[7] Geometry optimizations were run with unrestricted DFT calculations at the PBE level of theory using a 6-31G* basis set.[8–11] Solvation effects were considered using conductor-like polarizable continuum model (C-PCM).[12] TD-DFT calculations were performed using B3LYP level of theory using a 6-31G* basis set. Ten excited states were considered and calculated for both singlet and triplet transitions.[13] Solvation effects were considered for all optimization and single point energy calculation employed dichloromethane (8.93)[14] as the model solvent, while acetonitrile (36.65)[14] was used for TD-DFT calculations as this was the solvent used for experimental UV-Vis spectroscopy experimentation. No substantial differences in the geometric values were observed upon comparing geometry optimization calculations in vacuum or with C-PCM solvent considerations. Atomic van der Waal radii used in C-PCM calculation were considered employing universal force field (UFF) values.[15]

Synthetic Methods

Synthesis of $[Co_3(triphos)_3(THT)][BF_4]_3$ (1^{3+})

Solids $[Co(CH_3CN)_6][BF_4]_2$ (155 mg, 0.323 mmol), and 1,1,1-tris(diphenylphosphinomethyl)ethane (triphos) (194 mg, 0.310 mmol), along with 25 mL of acetonitrile were added to a 250 mL Schlenk flask under N_2. The reaction was stirred at room temperature for 1 hour, during which the mixture turned a lime green color. After one hour, triphenylene-2,3,6,7,10,11-hexathiol (THT) (45 mg, 0.107 mmol) and triethylamine (300 µL, 2.15 mmol) were added to the reaction mixture. After stirring at room temperature for two hours, a rust red precipitate formed. After an additional 12 hours of stirring, the reaction vessel was exposed to room atmosphere with ample mixing and bubbling using compressed atmospheric air, and the red precipitate dissolved, forming a blue solution. The mixture was first vacuum filtered, and the solvent of the filtrate was subsequently removed under vacuum, yielding a blue powder. The blue powder was washed with ~700 mL of cold THF and recrystallized by vapor diffusion of diethyl ether into an acetonitrile solution, to generate dark blue crystals in 80% yield. ^{1}H NMR (500 MHz, DMSO-d_6): δ 9.93 (s, 2H, $C_{18}H_6S_6$), 7.29 (t, 6H, $P(C_6H_5)_2$), 7.18 (m, 12H, $P(C_6H_5)_2$)), 7.10 (t, 12H, $P(C_6H_5)_2$), 2.98 (s, 6H, PCH_2), 2.00 (s, 3H, CH_3). ^{31}P-{^{1}H} NMR (202 MHz, DMSO-d_6): δ 33.8 (br s). ^{19}F-{^{1}H} NMR (470 MHz, DMSO-d_6): δ -148.0 (m). Elem. Anal. Calcd for $C_{141}H_{123}Co_3P_9S_6B_3F_{12}$: C 62.13; H 4.55. Found: C 60.86; H 4.88.

Synthesis of $[Co_3(triphos)_3(BHT)][BF_4]_3$ (2^{3+})

Solids $[Co(CH_3CN)_6][BF_4]_2$ (343 mg, 0.718 mmol), and 1,1,1-tris(diphenylphosphinomethyl)ethane (triphos) (625 mg, 0.643 mmol), along with 20 mL of acetonitrile were added to a 250 mL Schlenk flask under N_2. The reaction was stirred at room temperature for 1 hour, during which the mixture turned a lime green color. After one hour, benzenehexathiol (BHT) (271 mg, 0.248 mmol) and triethylamine (300 µL, 2.15 mmol) were added to the reaction mixture. After stirring at room temperature for two hours, the solution turned a blue-green color. After 12 hours of stirring, the reaction vessel was exposed to room atmosphere with ample mixing and bubbling using compressed atmospheric air, and the solution slowly turned more blue in color. The mixture was first vacuum filtered, and the solvent of the filtrate was subsequently removed under vacuum, yielding a blue powder. The blue powder was washed with ~700 mL of cold THF and recrystallized by vapor diffusion of diethyl ether into an acetonitrile solution, to generate dark blue crystals in 76% yield. ^{1}H NMR (500 MHz, DMSO-d_6): 7.20 (t, 6H, $P(C_6H_5)_2$), 7.15 (m, 12H, $P(C_6H_5)_2$), 6.88 (t, 12H, $P(C_6H_5)_2$), 2.97 (s, 6H, PCH_2), 2.01 (s, 3H, CH_3). ^{31}P-{^{1}H} NMR (202 MHz, DMSO-d_6): δ 31.4 (br s). ^{19}F-{^{1}H} NMR (470 MHz, DMSO-d_6): δ -148.0 (m). Elem. Anal. Calcd for $C_{129}H_{117}Co_3P_9S_6B_3F_{12}$: C 60.16; H 4.58. Found: C 59.73; H 4.74.

Synthesis of [Co(triphos)(BDT)][BF_4] (3^+)

The complex was synthesized using the reported procedure and was adapted to accommodate tetrafluoroborate as the counterion herein.[16] To a 250 mL flask under N_2, 411 mg (0.5 mmol) of the synthesized cobalt[1,1,1-tris(diphenylphosphinomethyl)ethane][benzene-1,2-dithiolate] (complex Co(triphos)(BDT), where triphos = 1,1,1-tris(diphenylphosphinomethyl)ethane, and BDT = benzene-1,2-dithiolate), 136 mg (0.5 mmol) of ferrocenium tetrafluoroborate ($FcBF_4$), and 50 mL of dichloromethane were added, yielding a violet solution. The reaction was stirred for 2 hr at room temperature. The mixture was transferred to a 1 L flask and stirred vigorously with ~ 700 mL of hexanes, yielding a purple precipitate, which was isolated by vacuum filtration and washed with copious amounts of hexanes. The product was recrystallized by vapor diffusion of diethyl ether into an acetonitrile solution, to generate violet crystals in 87% yield. ^{1}H NMR (500 MHz, DMSO-d_6) δ 8.29 (m, 2H, $C_6H_4S_2$), δ 7.55 (m, 2H, $C_6H_4S_2$), 7.26-7.05 (m, 30H, $P(C_6H_5)_2$), 2.95 (s, 6H, PCH_2), 1.98 (s, 3H, CH_3). ^{31}P-{^{1}H} NMR (202 MHz, DMSO-d_6) δ 33.9 (s). ^{19}F-{^{1}H} NMR (470 MHz, DMSO-d_6): δ -148.0 (m). Elem. Anal. Calcd for $C_{47}H_{43}CoP_3S_2BF_4$: C 61.99; H 4.76. Found: C 61.68; H 4.71.

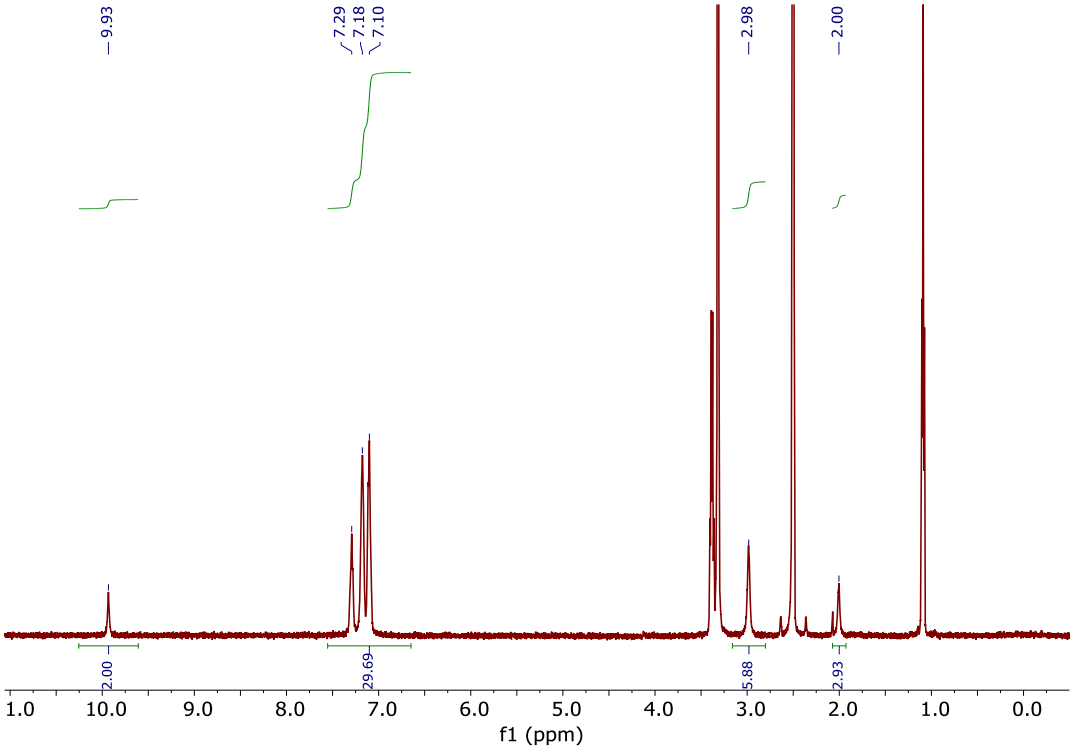

Figure S1. 500 MHz ^{1}H NMR spectrum of $\mathbf{1}^{3+}$ in dimethylsulfoxide-d_6.

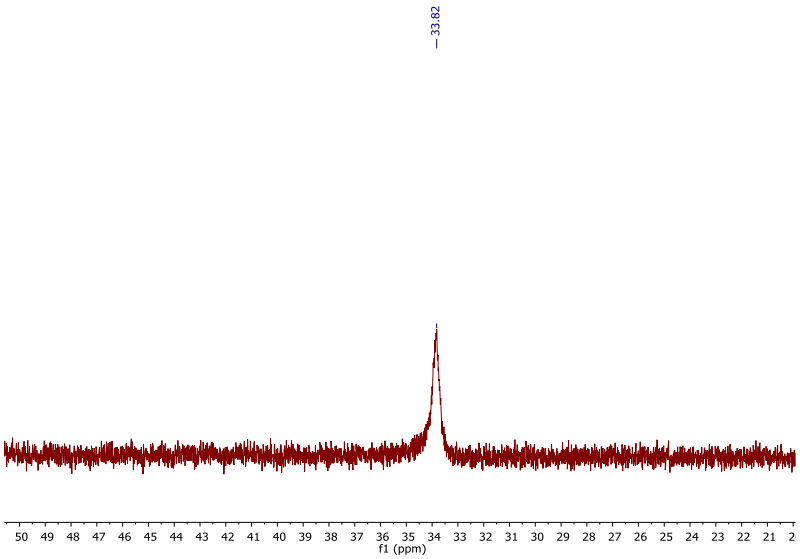

Figure S2. 202 MHz ^{31}P-{^{1}H} NMR spectrum of $\mathbf{1}^{3+}$ in dimethylsulfoxide-d_6.

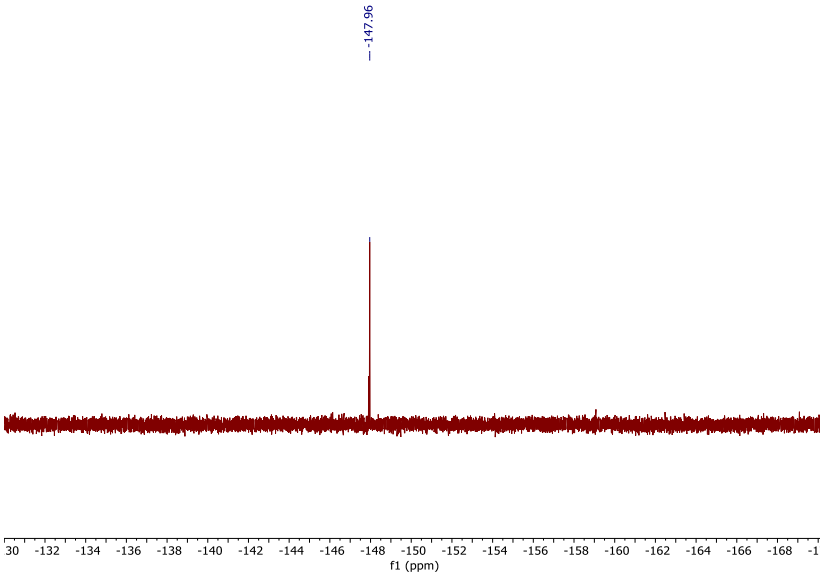

Figure S3. 470 MHz ^{19}F-{^{1}H} NMR spectrum of $\mathbf{1}^{3+}$ in dimethylsulfoxide-d_6.

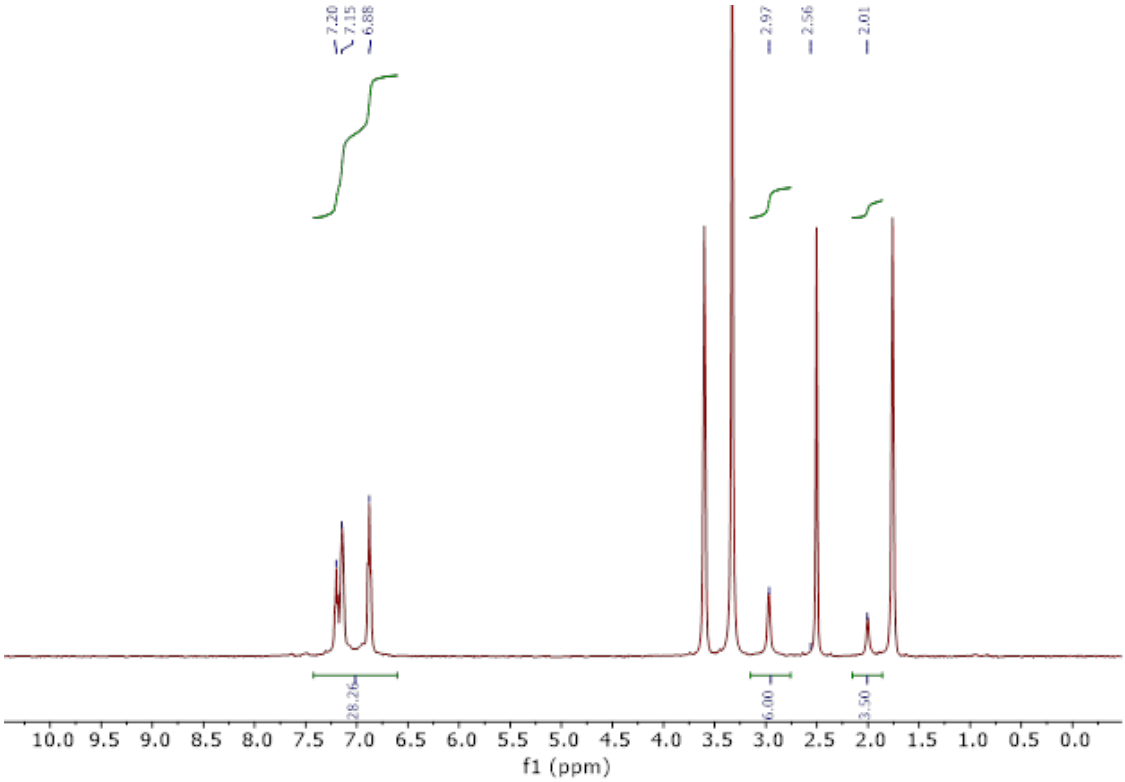

Figure S4. 500 MHz ^{1}H NMR spectrum of $\mathbf{2}^{3+}$ in dimethylsulfoxide-d_6.

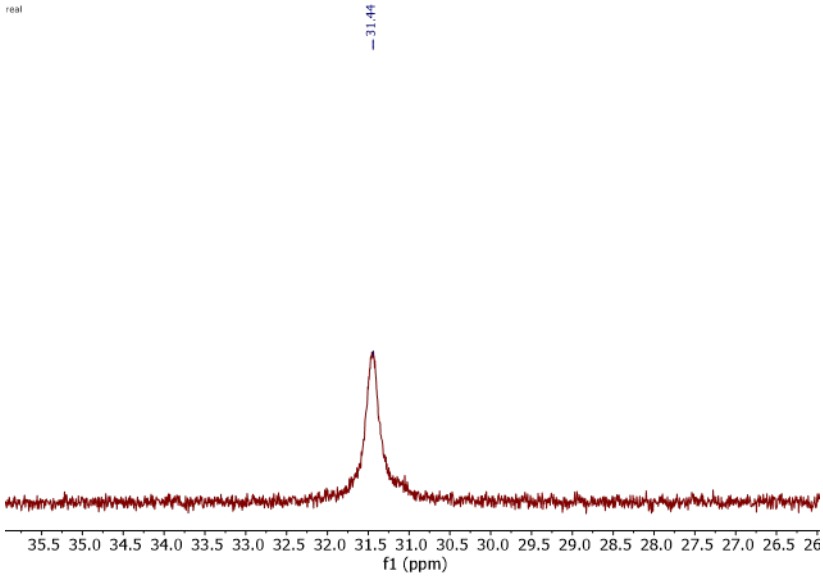

Figure S5. 202 MHz ^{31}P-{^{1}H} NMR spectrum of $\mathbf{2}^{3+}$ in dimethylsulfoxide-d_6.

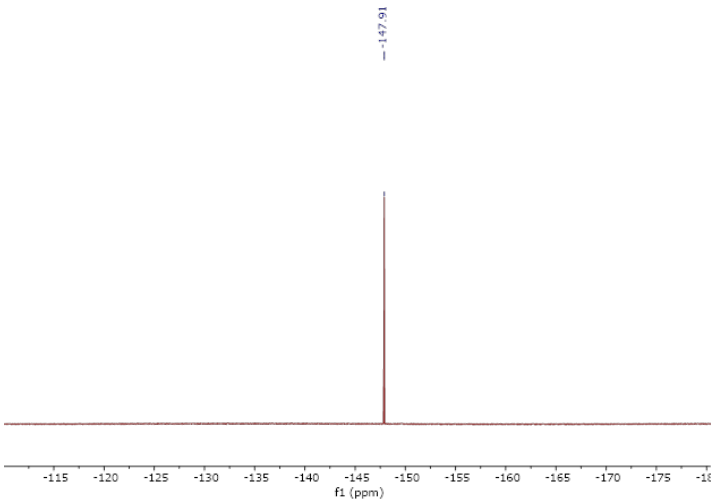

Figure S6. 470 MHz ^{19}F-{^{1}H} NMR spectrum of $\mathbf{2}^{3+}$ in dimethylsulfoxide-d_6.

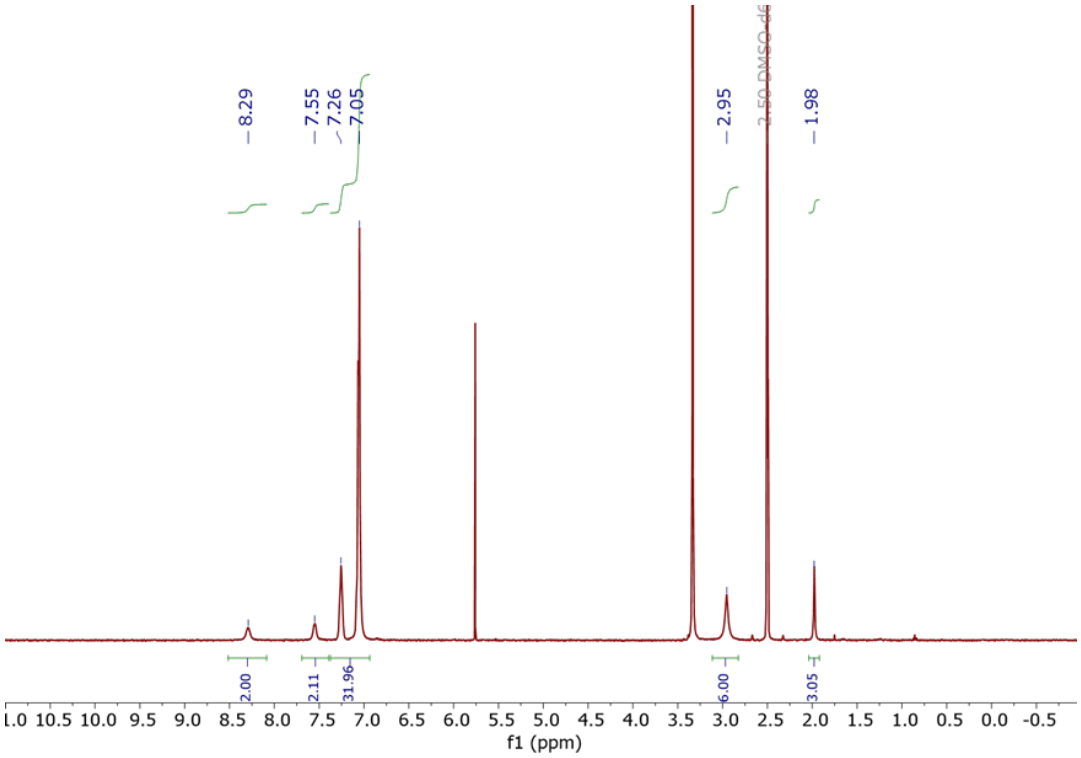

Figure S7. 500 MHz ^{1}H NMR spectrum of $\mathbf{3}^{+}$ in dimethylsulfoxide-d_6.

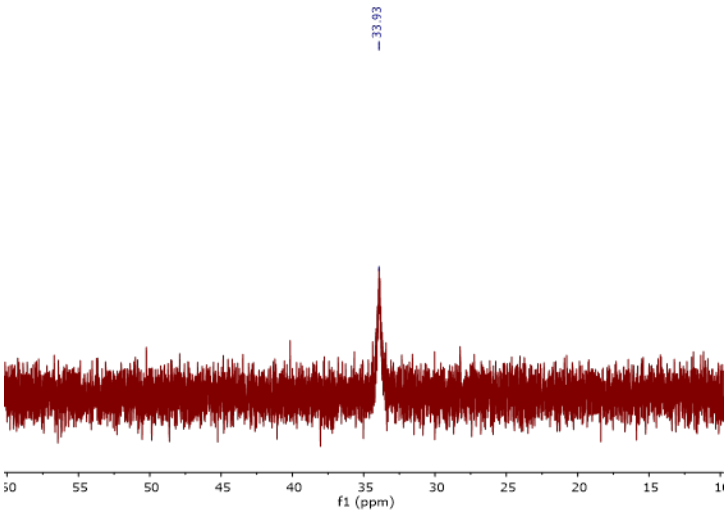

Figure S8. 202 MHz ^{31}P-{^{1}H} NMR spectrum of **3**$^{+}$ in dimethylsulfoxide-d_6.

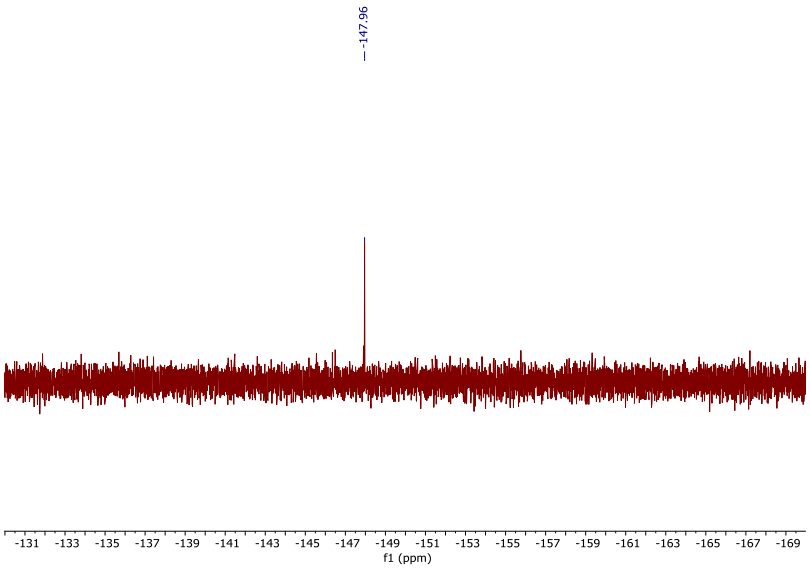

Figure S9. 470 MHz ^{19}F-{^{1}H} NMR spectrum of **3**$^{+}$ in dimethylsulfoxide-d_6.

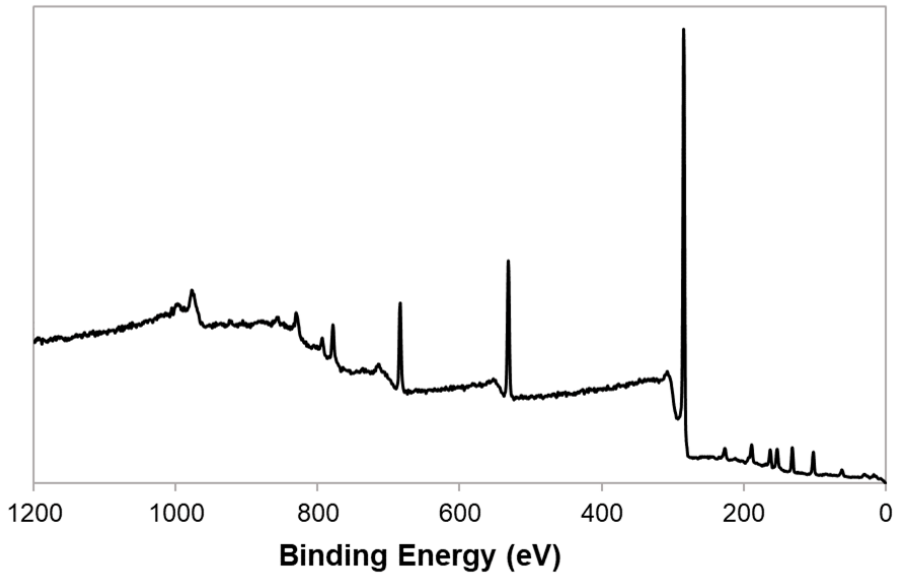

Figure S10. XPS survey scan of complex $\mathbf{1}^{3+}$.

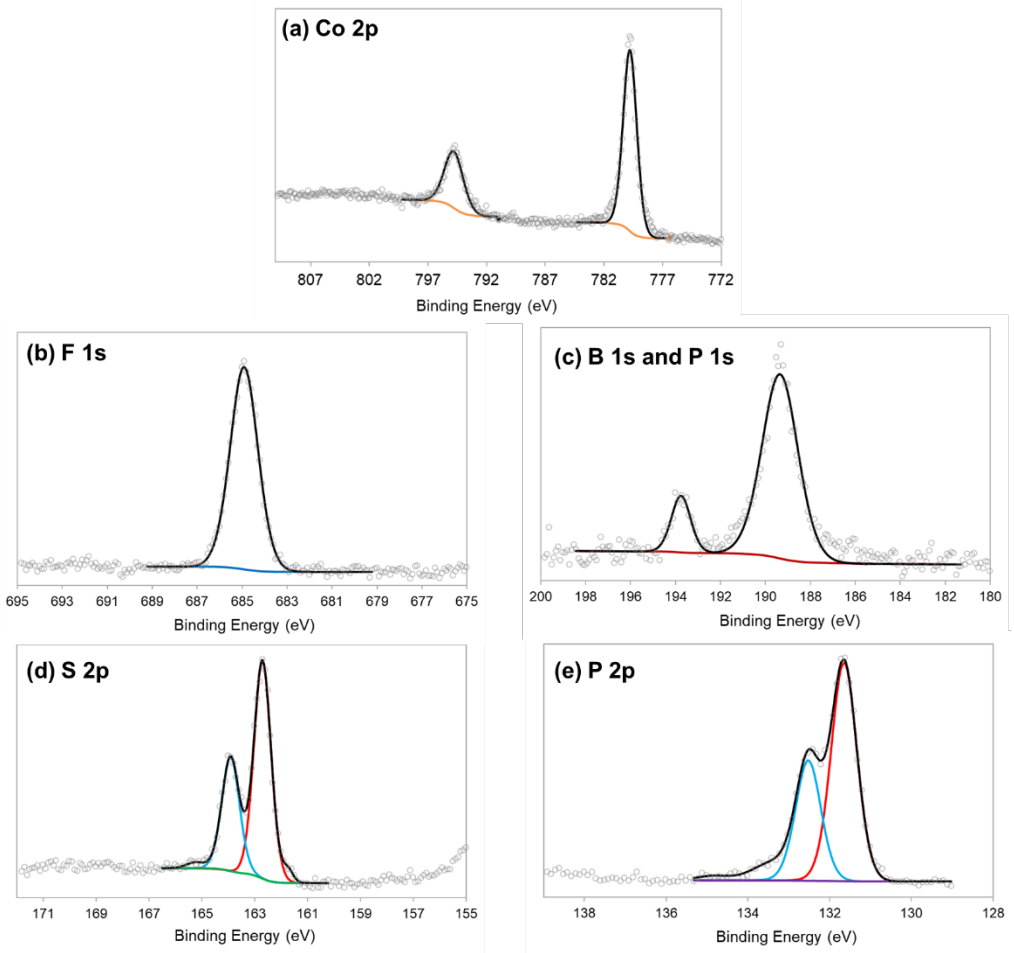

Figure S11. High-resolution X-ray photoelectron spectroscopy spectra of the a) Co 2p region; b) F 1s region; c) B 1s and P 1s region; d) S 2p region; e) P 2p region for complex $\mathbf{1}^{3+}$.

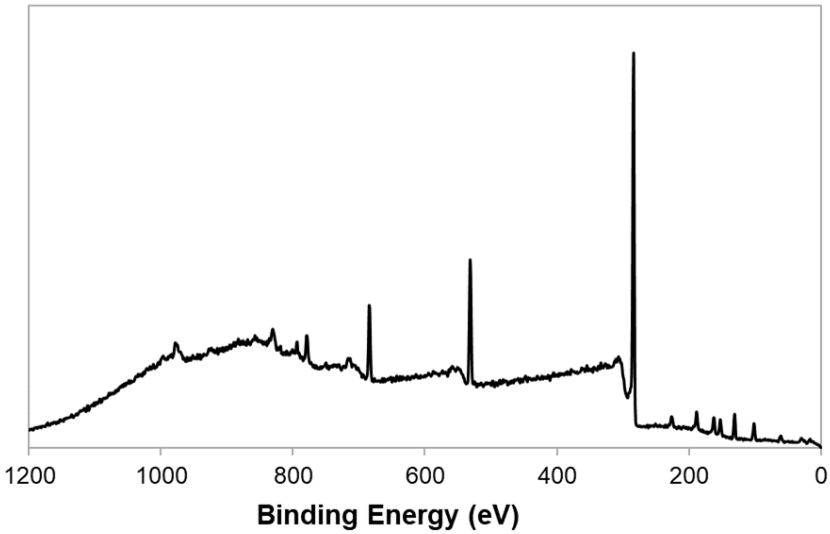

Figure S12. XPS survey scan of complex $\mathbf{2}^{3+}$.

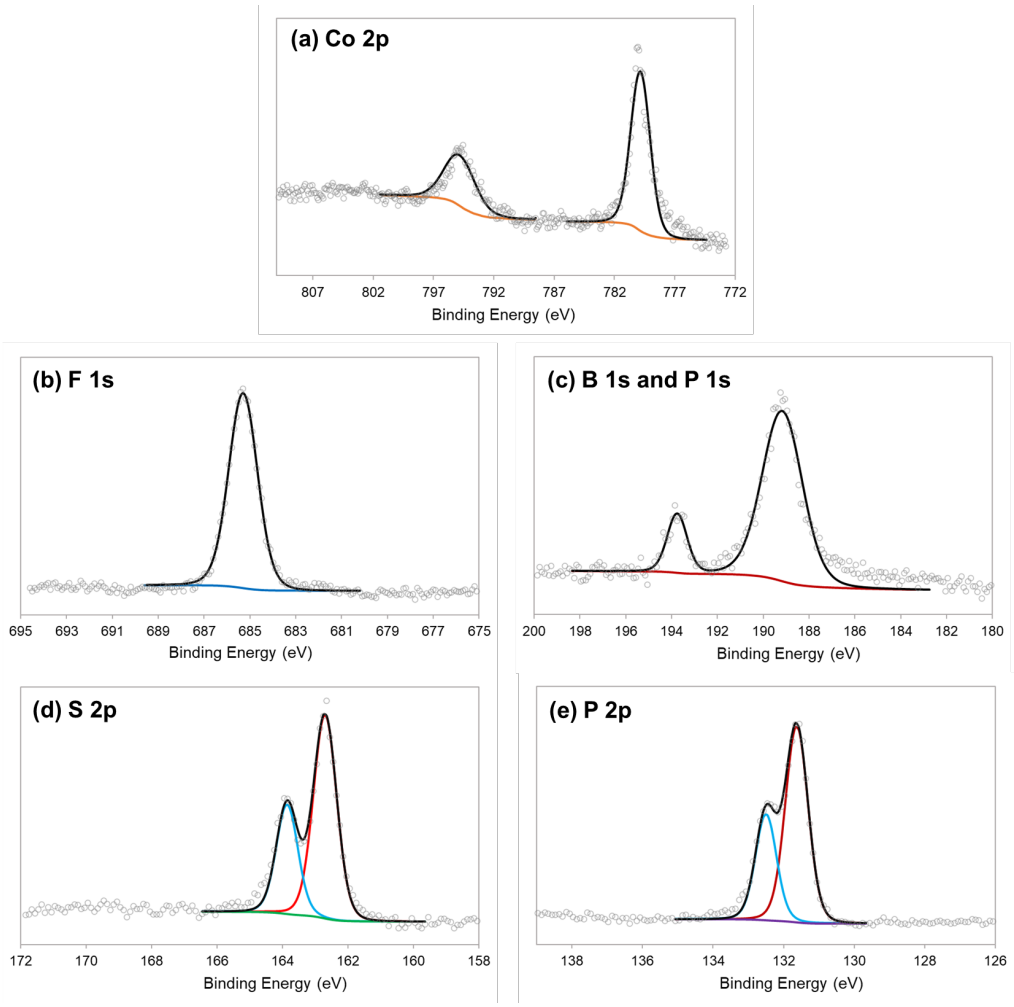

Figure S13. High-resolution X-ray photoelectron spectroscopy spectra of the a) Co 2p region; b) F 1s region; c) B 1s and P 1s region; d) S 2p region; e) P 2p region for complex $\mathbf{2}^{3+}$.

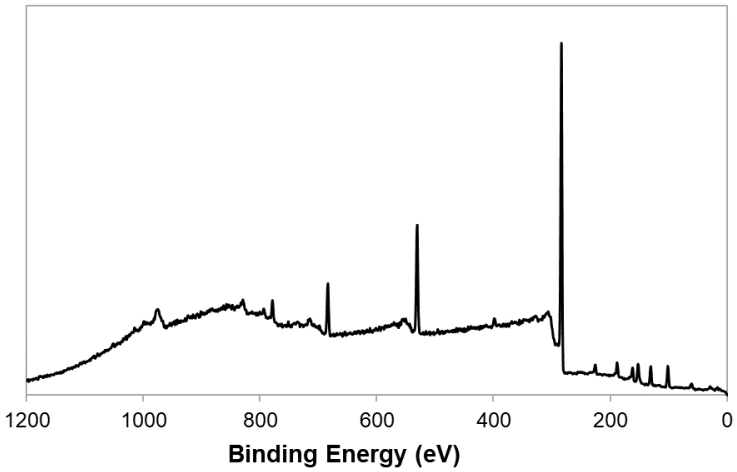

Figure S14. XPS survey scan of complex $\mathbf{3}^{+}$.

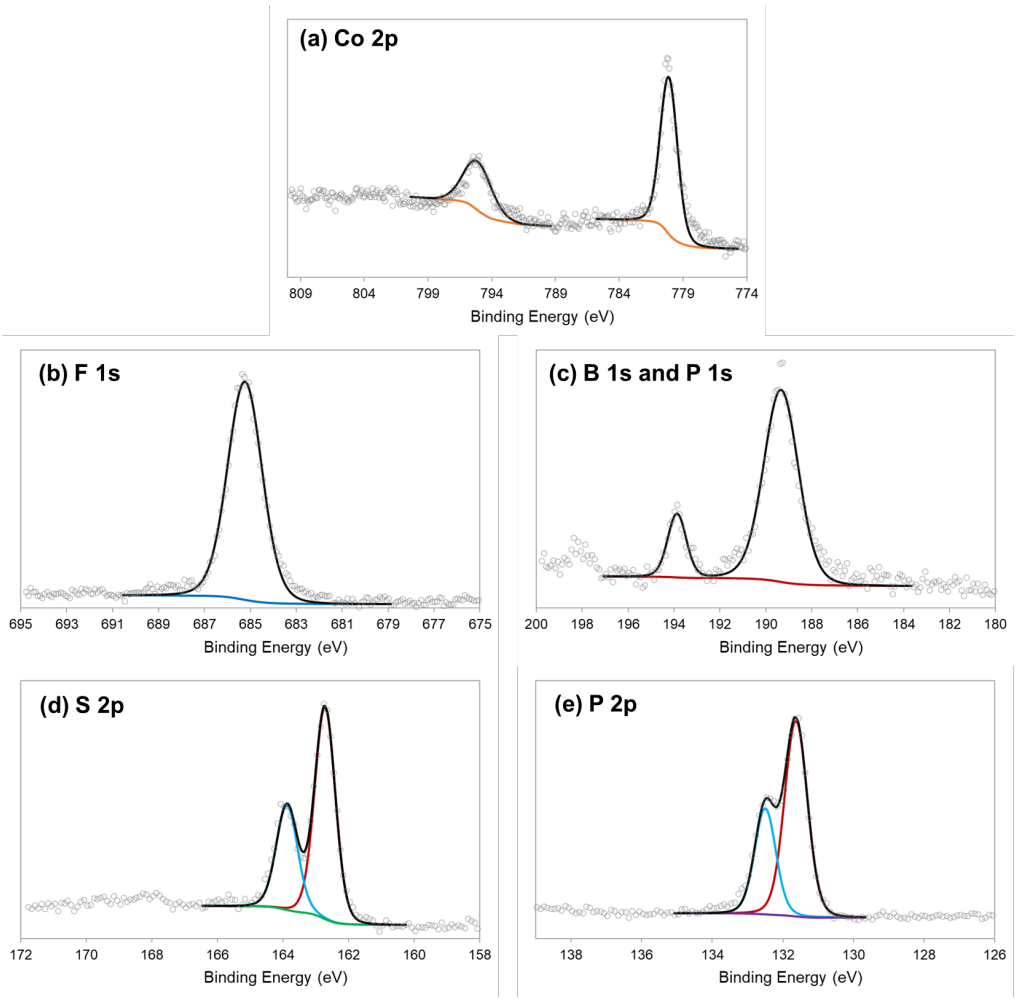

Figure S15. High-resolution X-ray photoelectron spectroscopy spectra of the a) Co 2p region; b) F 1s region; c) B 1s and P 1s region; d) S 2p region; e) P 2p region for complex $\mathbf{3}^{+}$.

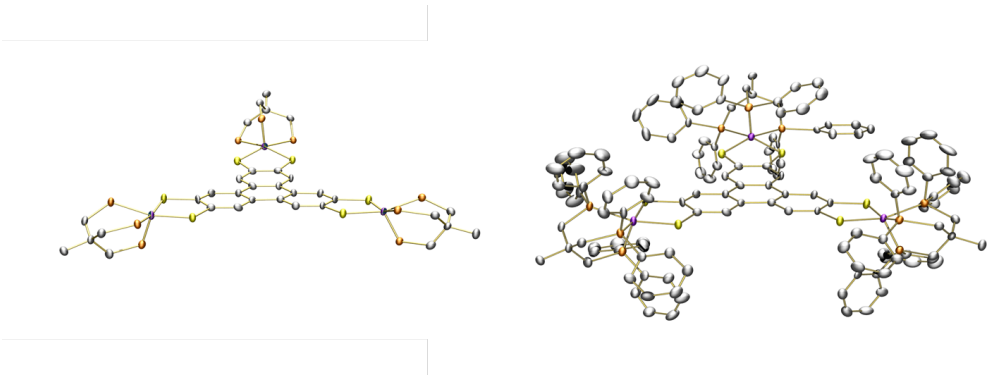

Figure S16. Top down views of the solid-state structure of $\mathbf{1}^{3+}$. Aryl and aliphatic protons, counterions, and solvent molecules are omitted for clarity.

Figure S17. Side view of the solid-state structure of $\mathbf{1}^{3+}$. Aryl and aliphatic protons, counterions, and solvent molecules are omitted for clarity.

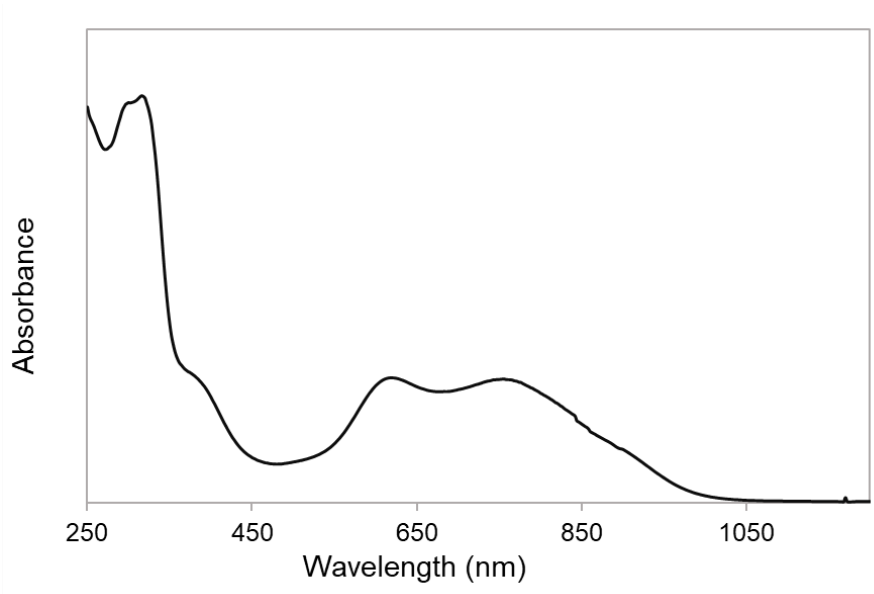

Figure S18. UV/-vis spectrum of 0.025 mM of $\mathbf{1}^{3+}$ in acetonitrile.

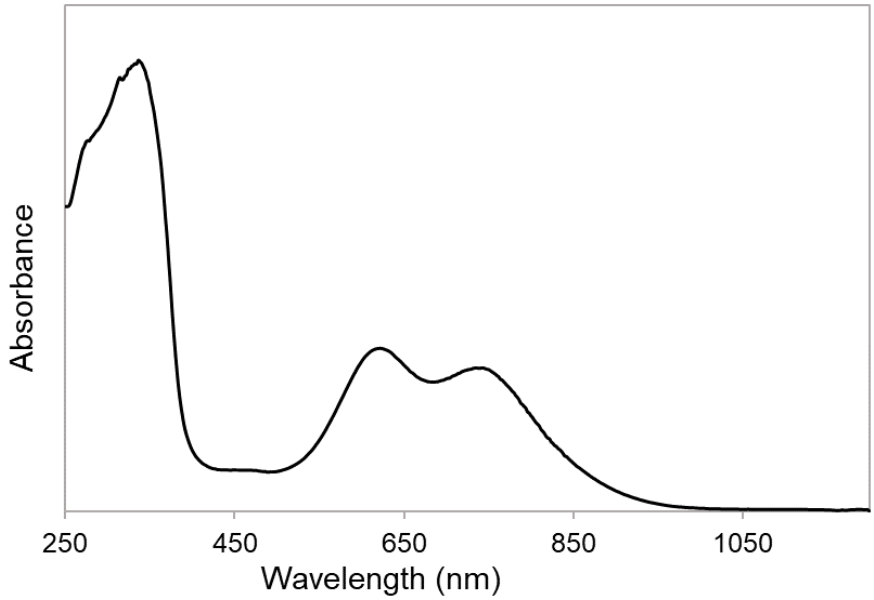

Figure S19. UV-vis spectrum of 0.025 mM of $\mathbf{2}^{3+}$ in acetonitrile.

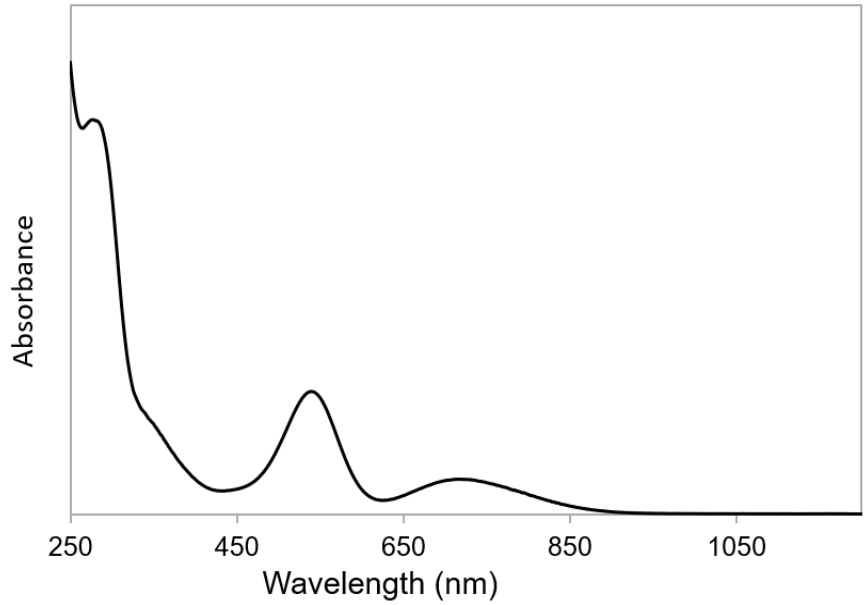

Figure S20. UV/-vis spectrum of 0.1 mM of $\mathbf{3}^{+}$ in acetonitrile.

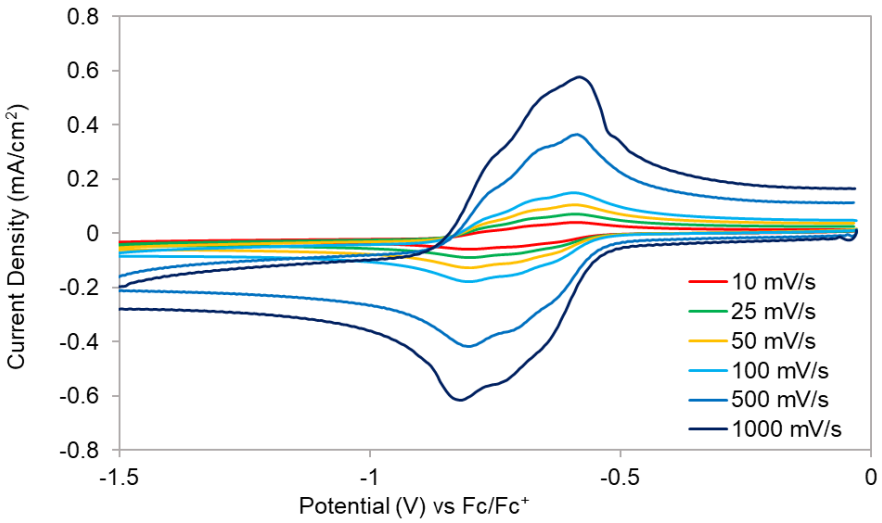

Figure S21. Cyclic voltammograms of 0.5 mM of **1** in a CH_3CN solution containing 0.1 M [nBu$_4$N][PF_6] under an atmosphere of N_2. Scan rates vary from 10 to 1000 mV/s.

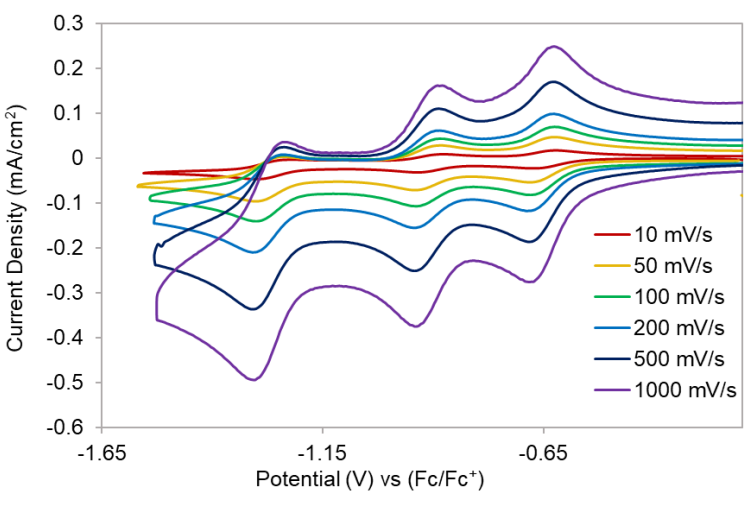

Figure S22. Cyclic voltammograms of 0.5 mM of **2** in a CH_3CN solution containing 0.1 M [nBu$_4$N][PF_6] under an atmosphere of N_2. Scan rates vary from 10 to 1000 mV/s.

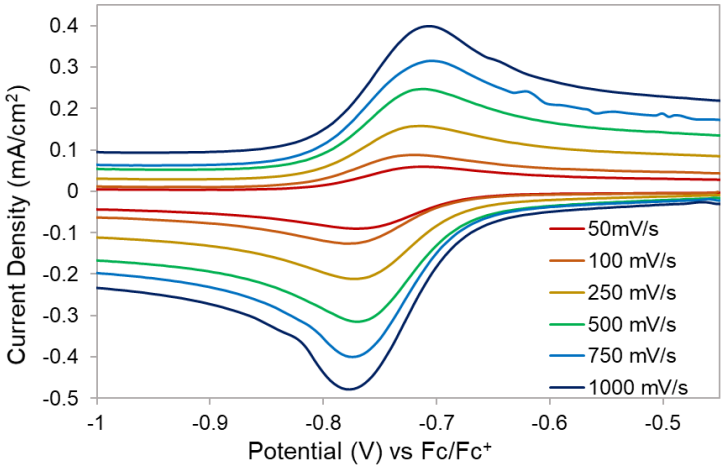

Figure S23. Cyclic voltammograms of 0.5 mM of **3** in a CH_3CN solution containing 0.1 M [nBu$_4$N][PF_6] under an atmosphere of N_2. Scan rates vary from 50 to 1000 V/s.

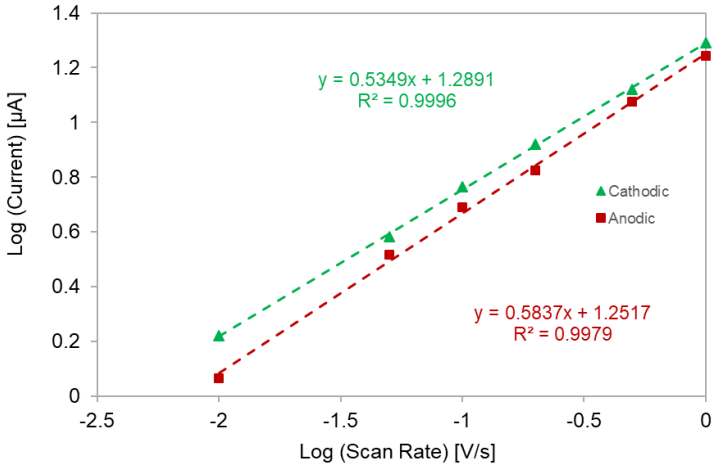

Figure S24. Plot of log of current density vs log of the scan rate for the first redox couple of **1** in MeCN. Current densities were measured at -0.822 V (cathodic) and -0.624 V (anodic) vs Fc/Fc^+.

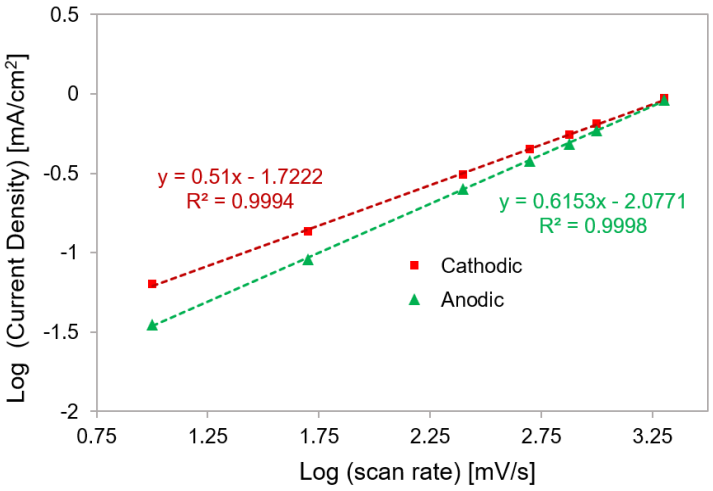

Figure S25. Plot of log of current density vs log of the scan rate for the first redox couple of **2** in MeCN. Current densities were measured at -0.673 V (cathodic) and -0.621 V (anodic) vs Fc/Fc^{+}.

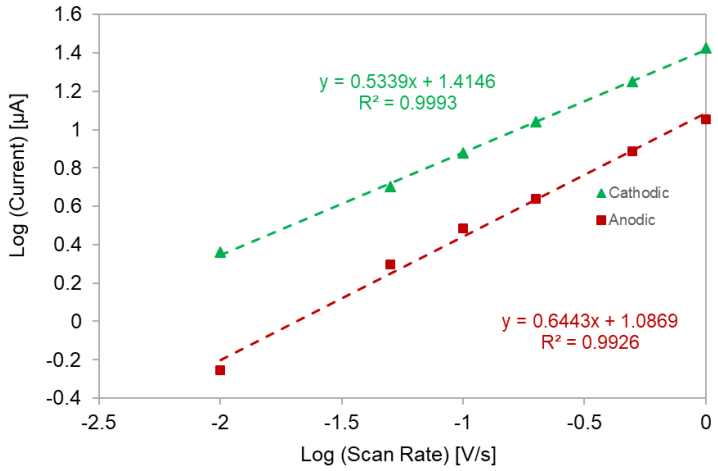

Figure S26. Plot of log of current density vs log of the scan rate for the second redox couple of **2** in MeCN. Current densities were measured at -0.938 V (cathodic) and -0.886 V (anodic) vs Fc/Fc^{+}.

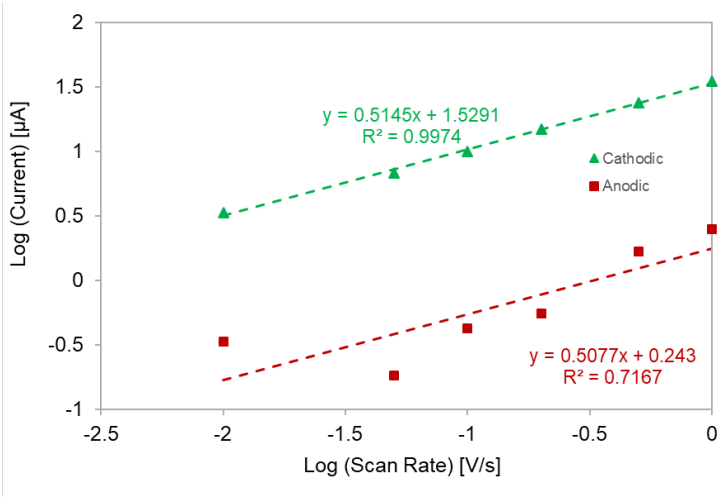

Figure S27. Plot of log of current density vs log of the scan rate for the third redox couple of **2** in MeCN. Current densities were measured at -1.30 V (cathodic) and -1.23 V (anodic) vs Fc/Fc^{+}.

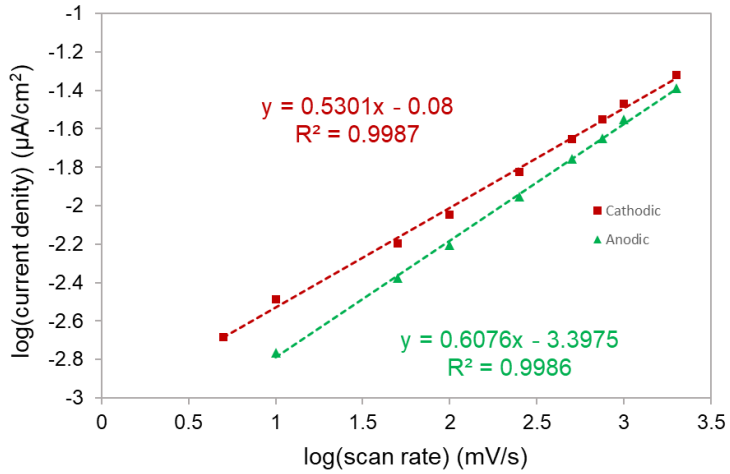

Figure S28. Plot of log of current density vs log of the scan rate for the redox couple of **3** in MeCN. Current densities were measured at -0.785 V (cathodic) and -0.724 V (anodic) vs Fc/Fc^{+}.

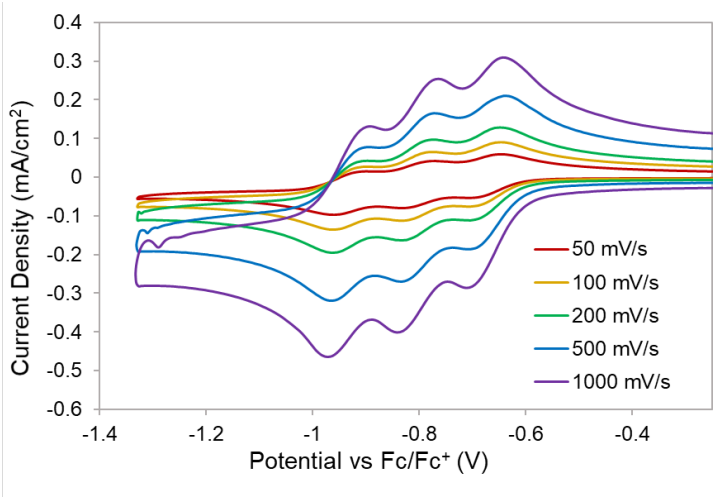

Figure S29. Cyclic voltammograms of 0.5 mM of **1** in a DCM solution containing 0.1 M [*n*Bu$_4$N][PF$_6$] under an atmosphere of N$_2$. Scan rates vary from 50 to 1000 mV/s.

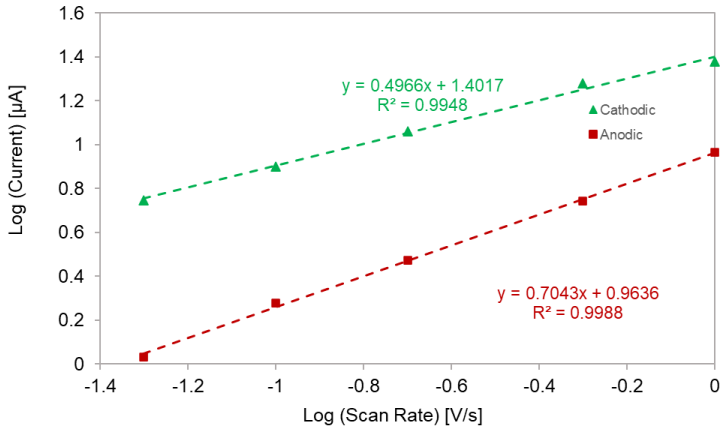

Figure S30. Plot of log of current density vs log of the scan rate for the first redox couple of **1** in DCM. Current densities were measured at -0.689 V (cathodic) and -0.642 V (anodic) vs Fc/Fc$^+$.

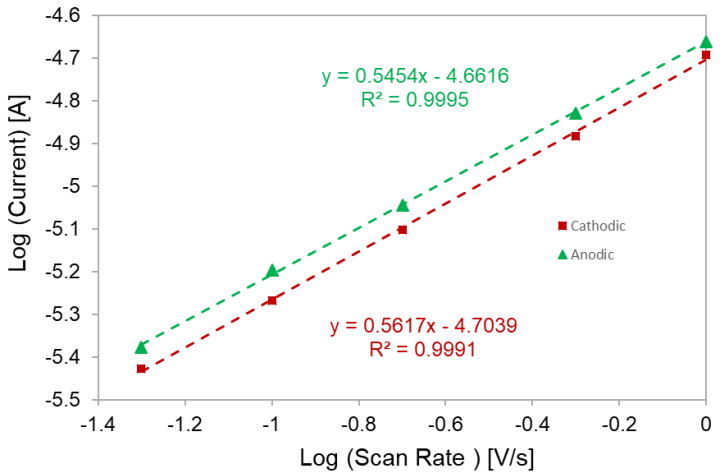

Figure S31. Plot of log of current density vs log of the scan rate for the second redox couple of **1** in DCM. Current densities were measured at -0.824 V (cathodic) and -0.777 V (anodic) vs Fc/Fc^{+}.

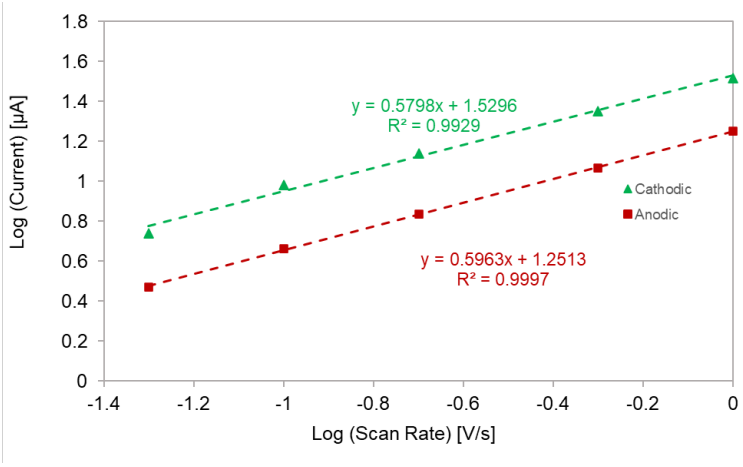

Figure S32. Plot of log of current density vs log of the scan rate for the third redox couple of **1** in DCM. Current densities were measured at -0.954 V (cathodic) and -0.907 V (anodic) vs Fc/Fc^{+}.

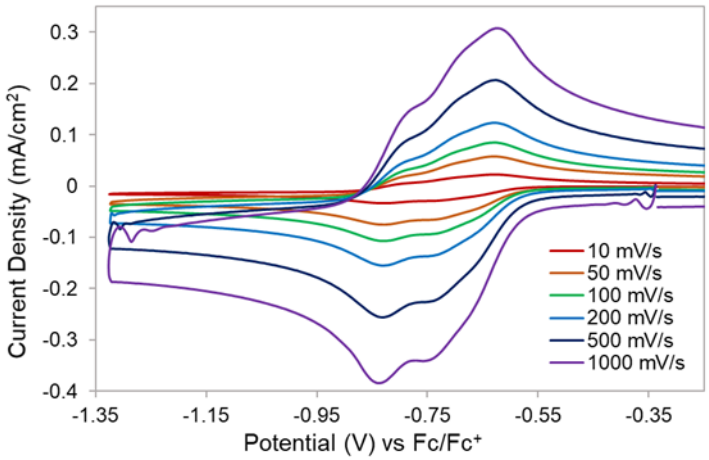

Figure S33. Cyclic voltammograms of 0.5 mM of **1** in a DMF solution containing 0.1 M [*n*Bu$_4$N][PF$_6$] under an atmosphere of N$_2$. Scan rates vary from 10 to 1000 mV/s.

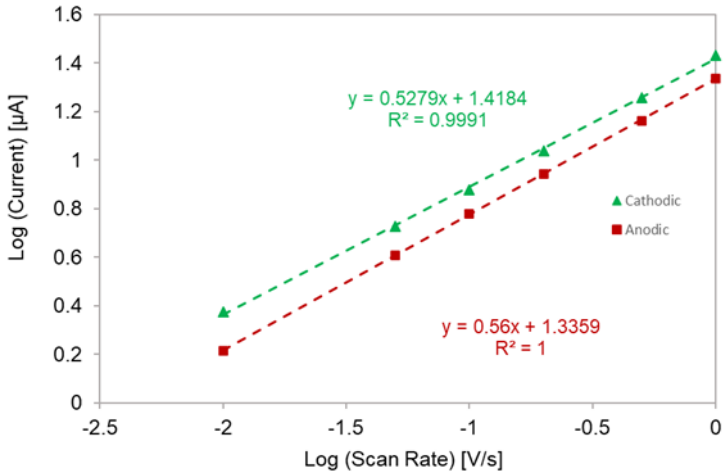

Figure S34. Plot of log of current density vs log of the scan rate for the first redox couple of **1** in DMF. Current densities were measured at -0.831 V (cathodic) and -0.611 V (anodic) vs Fc/Fc$^+$.

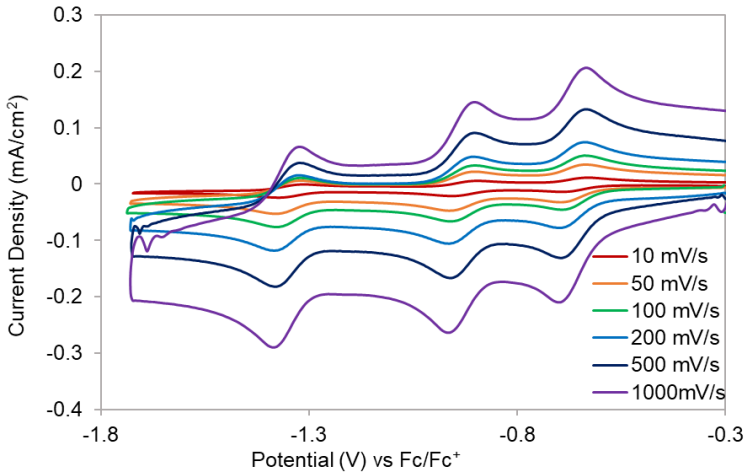

Figure S35. Cyclic voltammograms of 0.5 mM of **2** in a DMF solution containing 0.1 M [*n*Bu$_4$N][PF$_6$] under an atmosphere of N$_2$. Scan rates vary from 10 to 1000 mV/s.

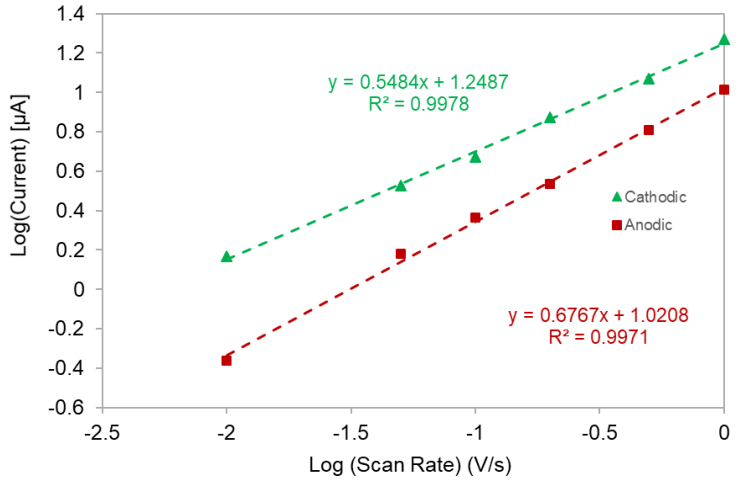

Figure S36. Plot of log of current density vs log of the scan rate for the first redox couple of **2** in DMF. Current densities were measured at -0.694 V (cathodic) and -0.630 V (anodic) vs Fc/Fc$^+$.

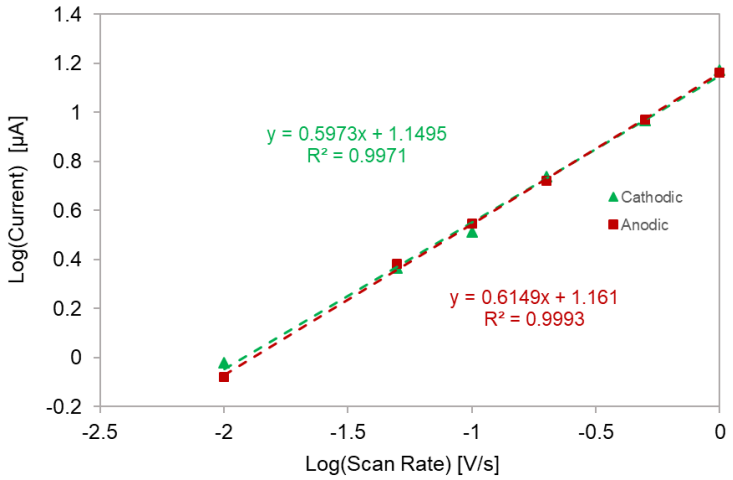

Figure S37. Plot of log of current density vs log of the scan rate for the second redox couple of **2** in DMF. Current densities were measured at -0.963 V (cathodic) and -0.896 V (anodic) vs Fc/Fc^{+}.

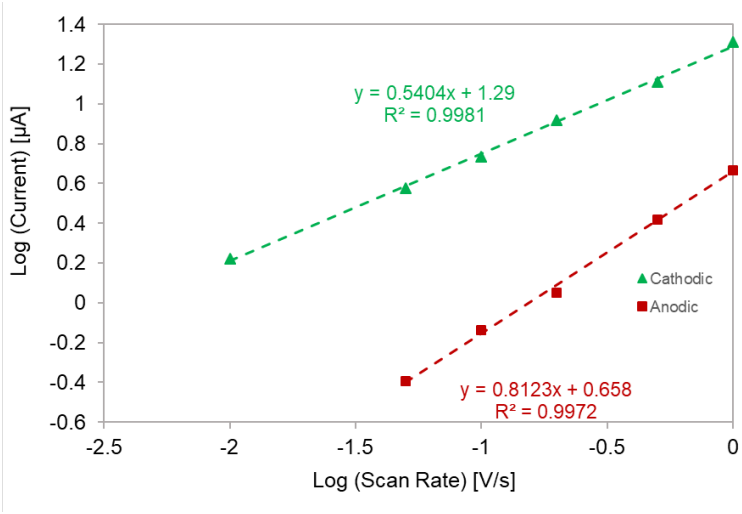

Figure S38. Plot of log of current density vs log of the scan rate for the third redox couple of **2** in DMF. Current densities were measured at -1.320 V (cathodic) and -1.370 V (anodic) vs Fc/Fc^{+}.

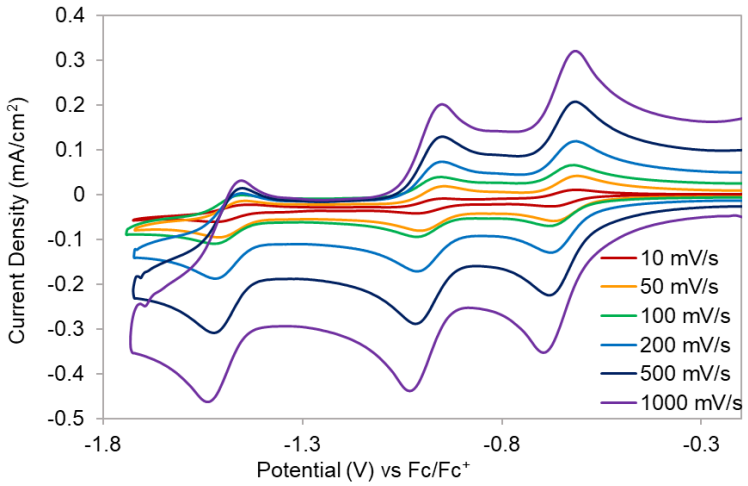

Figure S39. Cyclic voltammograms of 0.45 mM of **2** in a DCM solution containing 0.1 M [*n*Bu$_4$N][PF$_6$] under an atmosphere of N$_2$. Scan rates vary from 10 to 1000 mV/s.

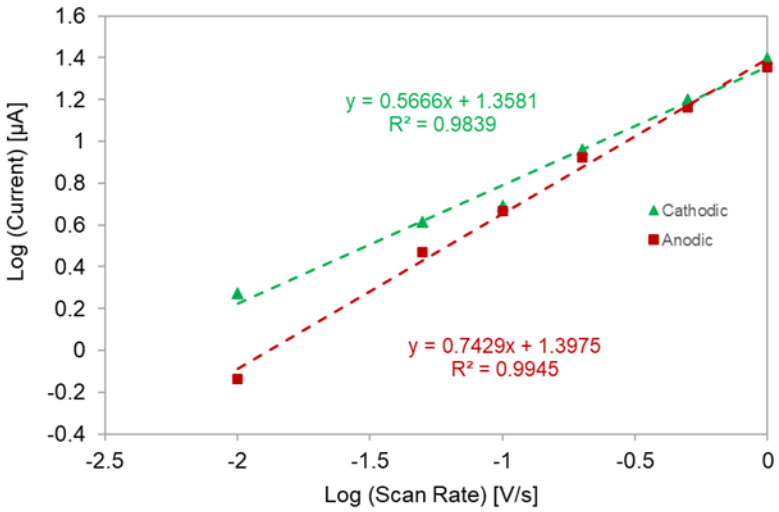

Figure S40. Plot of log of current density vs log of the scan rate for the first redox couple of **2** in DCM. Current densities were measured at -0.691 V (cathodic) and -0.613 V (anodic) vs Fc/Fc$^+$.

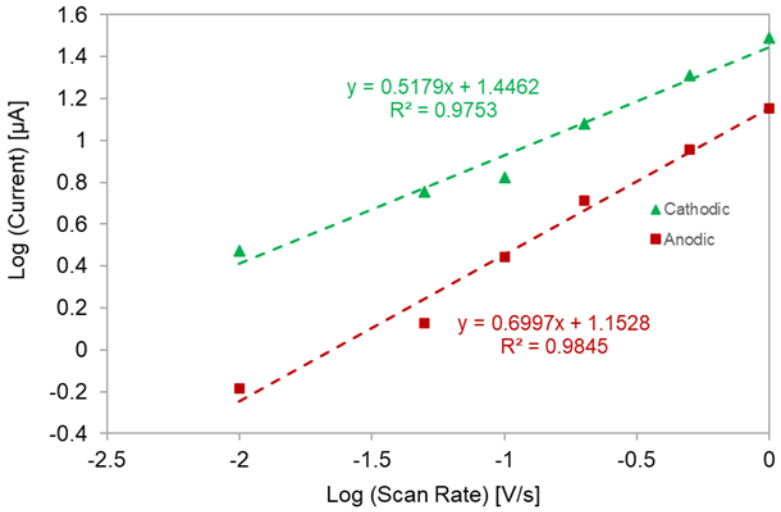

Figure S41. Plot of log of current density vs log of the scan rate for the second redox couple of **2** in DCM. Current densities were measured at -1.030 V (cathodic) and -0.942 V (anodic) vs Fc/Fc^{+}.

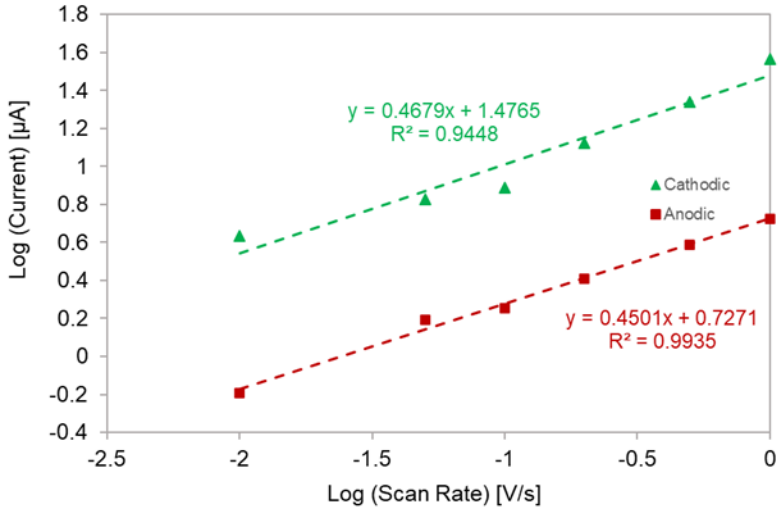

Figure S42. Plot of log of current density vs log of the scan rate for the third redox couple of **2** in DCM. Current densities were measured at -1.530 V (cathodic) and -1.480 V (anodic) vs Fc/Fc^{+}.

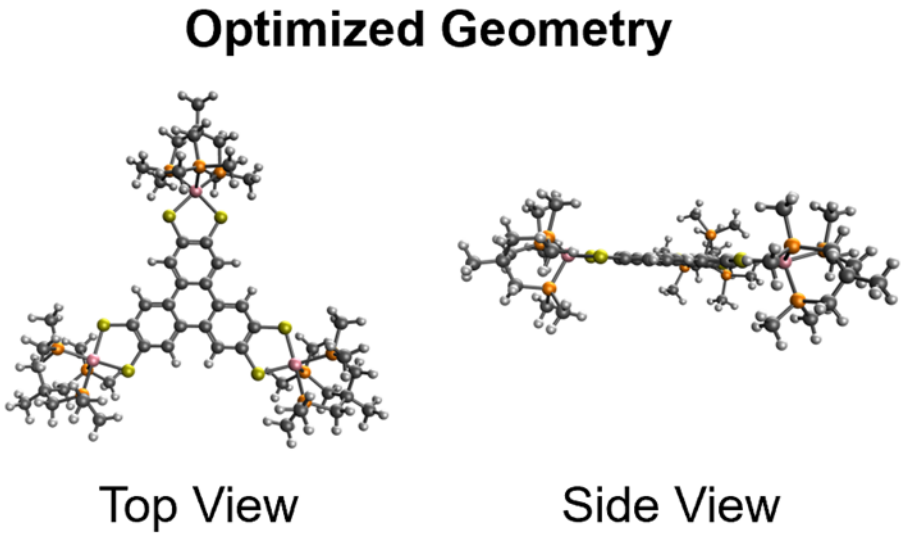

Figure S43. DFT optimized geometry of $\mathbf{1}^{3+}$ (aryl substituents of the triphos ligand exchanged for methyl moieties) (6-31G*/PBE level of theory).

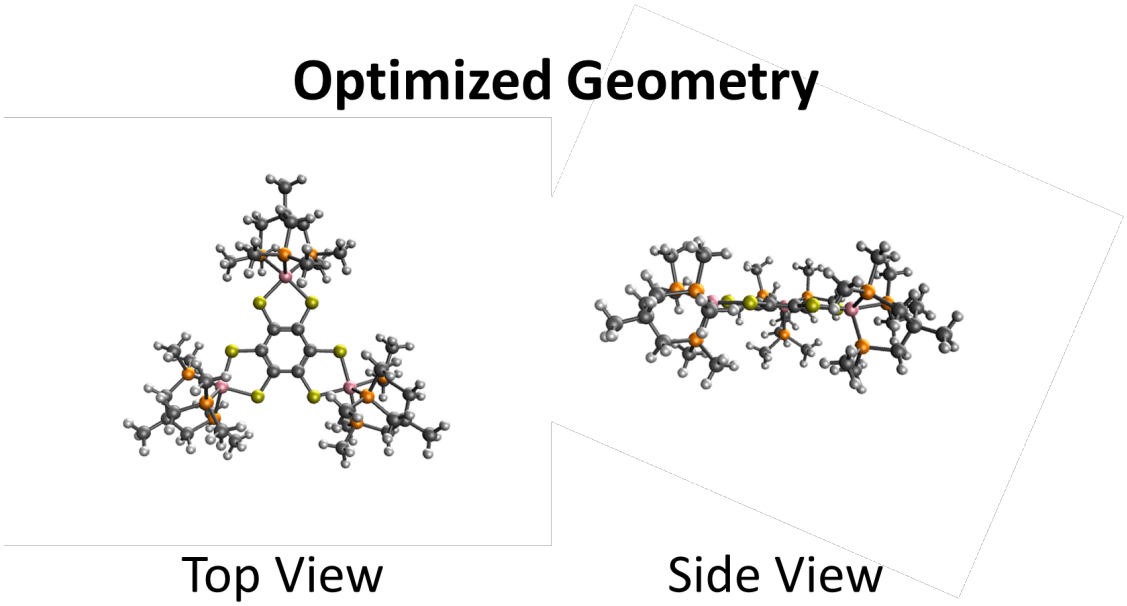

Figure S44. DFT optimized geometry of $\mathbf{2}^{3+}$ (aryl substituents of the triphos ligand exchanged for methyl moieties) (6-31G*/PBE level of theory).

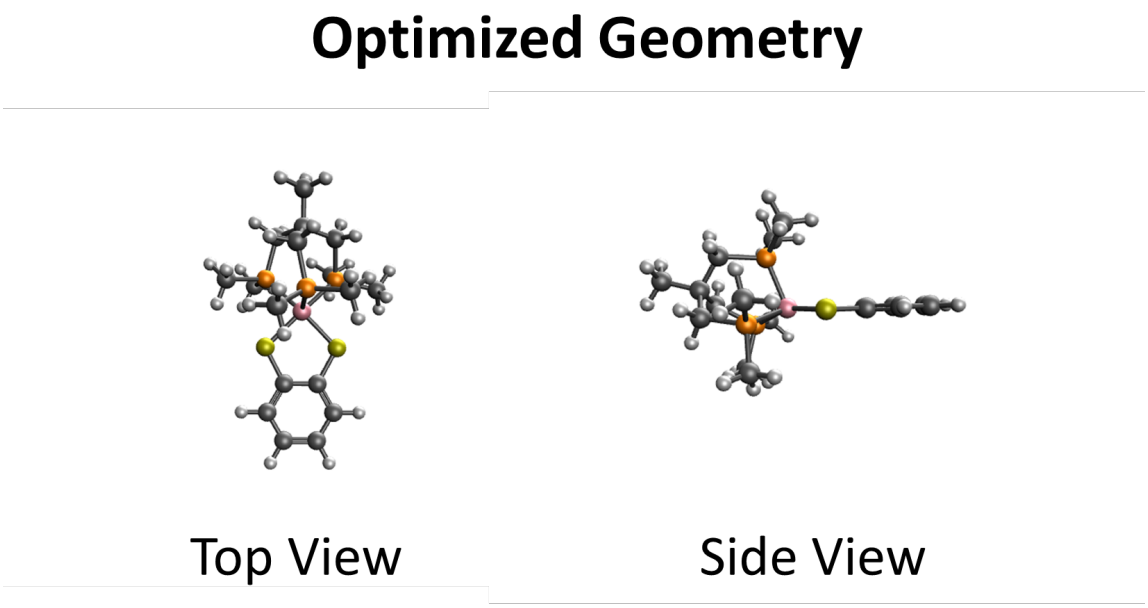

Figure S45. DFT optimized geometry of $\mathbf{3}^{+}$ (aryl substituents of the triphos ligand exchanged for methyl moieties) (6-31G*/PBE level of theory).

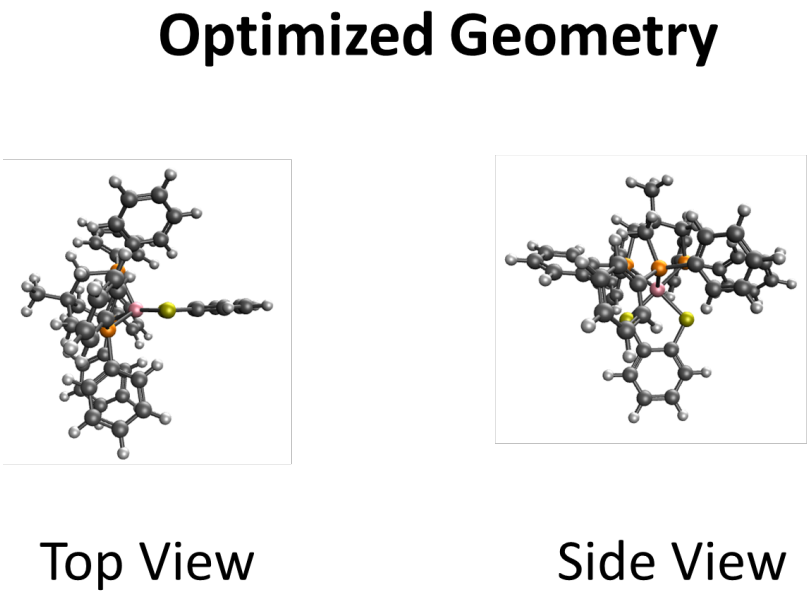

Figure S46. DFT optimized geometry of $\mathbf{3}^{+}$ (6-31G*/PBE level of theory).

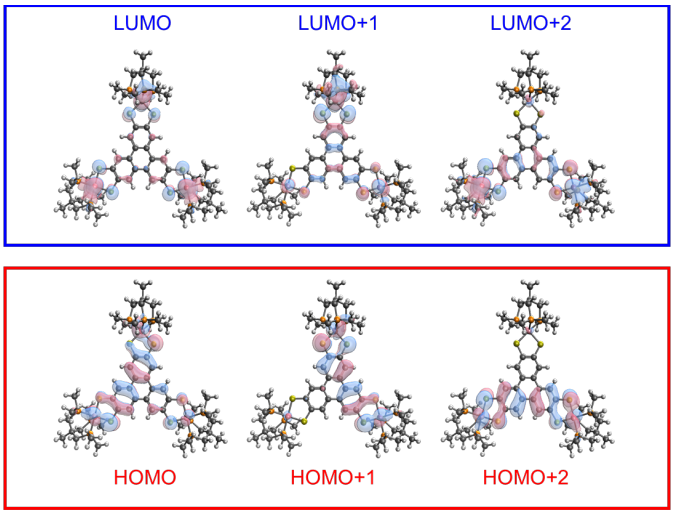

Figure S47. DFT calculated frontier orbitals for complex $\mathbf{1}^{3+}$ (6-31G*/PBE level of theory).

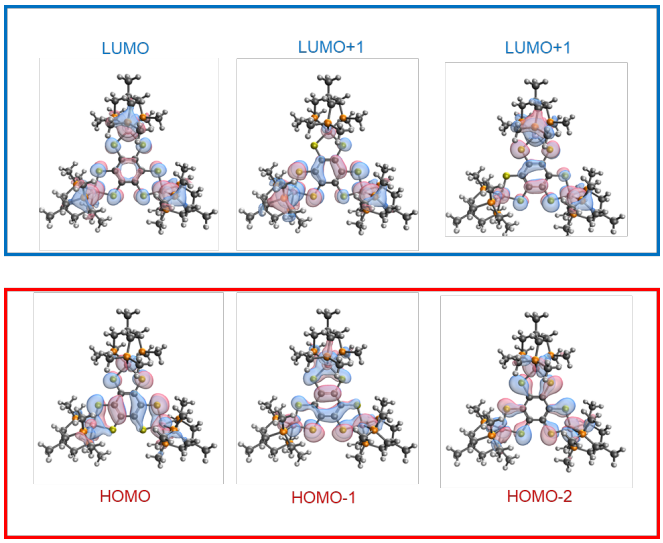

Figure S48. DFT calculated frontier orbitals for complex $\mathbf{2}^{3+}$ (6-31G*/PBE level of theory).

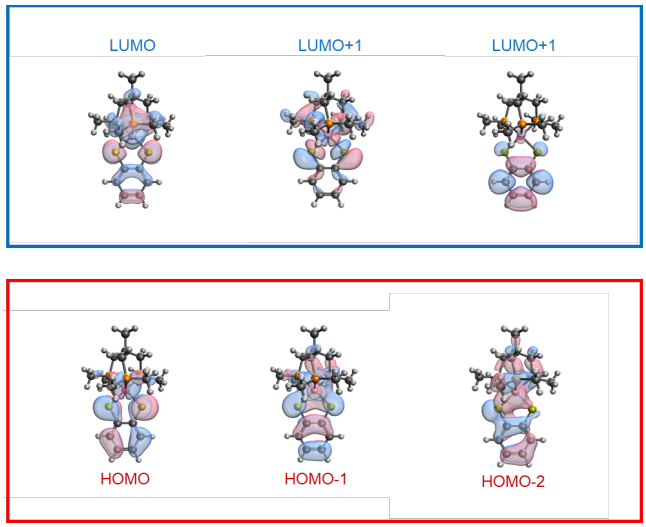

Figure S49. DFT calculated frontier orbitals for complex $\mathbf{3}^{+}$ (6-31G*/PBE level of theory).

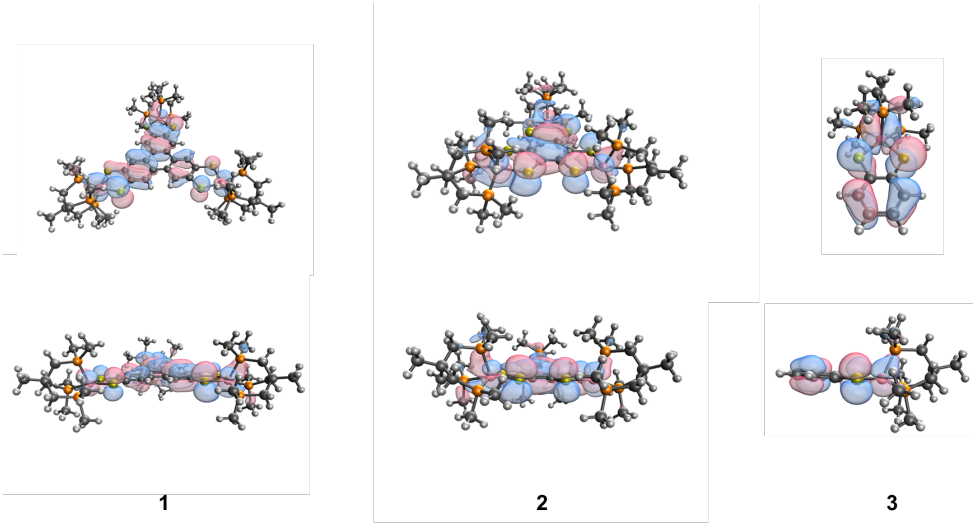

Figure S50. DFT calculated HOMO orbitals for complexes $\mathbf{1}^{3+}$, $\mathbf{2}^{3+}$, and $\mathbf{3}^{+}$ (6-31G*/PBE level of theory).

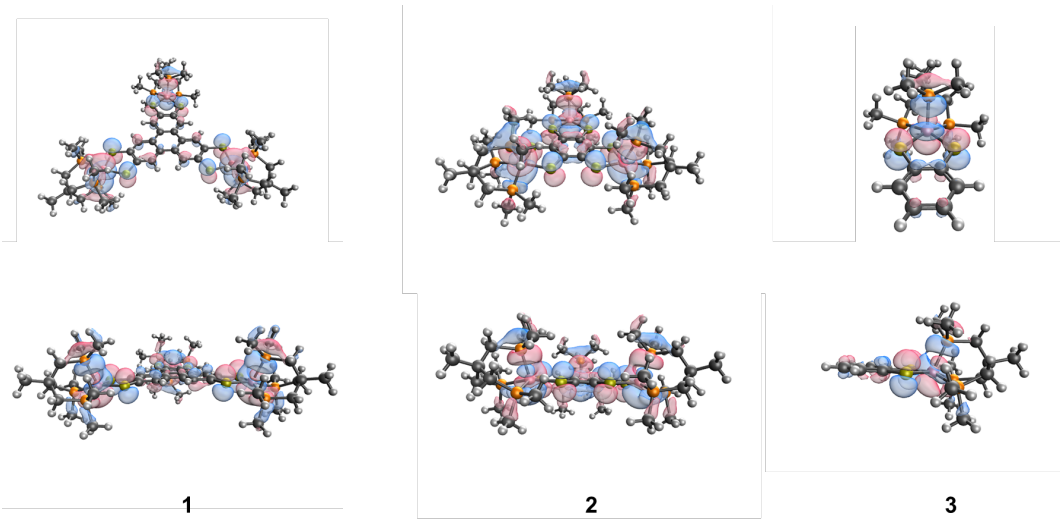

Figure S51. DFT calculated LUMO orbitals for complexes $\mathbf{1}^{3+}$, $\mathbf{2}^{3+}$, and $\mathbf{3}^{+}$ (6-31G*/PBE level of theory).

Table S1. DFT calculated orbital energies of frontier orbitals of complexes $\mathbf{1}^{3+}$, $\mathbf{2}^{3+}$, and $\mathbf{3}^{+}$.

Orbitals	Calculated Orbital Energy (eV)		
	Complex $\mathbf{1}^{3+}$	Complex $\mathbf{2}^{3+}$	Complex $\mathbf{3}^{+}$
LUMO+2	-4.14702	-4.16334	-1.31159
LUMO+1	-4.14974	-4.17151	-2.75107
LUMO	-4.23137	-4.32661	-3.86674
HOMO	-5.445	-5.5865	-5.34432
HOMO-1	-5.47221	-5.6246	-5.55385
HOMO-2	-5.49942	-5.80147	-6.15794

Table S2. TD-DFT calculated excited states for complex $\mathbf{3}^{+}$ and their associated excitation energy, wavelength, and oscillator strength.

Excited State	Excitation Energy (eV)	Wavelength (nm)	Oscillator Strength
1	1.5474	801.2149	0.0063
2	1.8375	674.7211	0.0167

3	2.4501	506.0202	0.0252
4	2.6771	463.1131	0.0792
5	2.7158	456.5137	0.0382
6	2.8492	435.1397	0.0145
7	2.9278	423.4579	0.0110
8	3.0549	405.8398	0.0065
9	3.1439	394.351	0.0060
10	3.1702	391.0794	0.0018

Table S3. Calculated relative contribution of transitions to excited state 4 of complex $\mathbf{3}^{+}$.

Transition	% contribution
HOMO-15 -> LUMO	10.96015
HOMO-11-> LUMO	13.18357
HOMO-3 -> LUMO	17.95751
HOMO-1 -> LUMO	13.73247
HOMO -> LUMO	44.1663

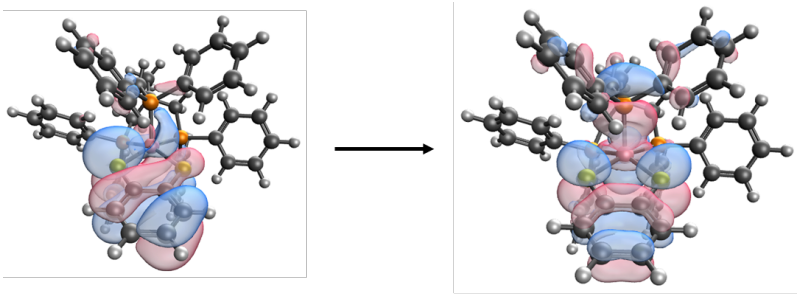

Figure S52. Origin of orbitals that highly contribute toward transition of excited state 4 in complex $\mathbf{3}^{+}$.

Table S4. Calculated relative contribution of transitions to excited state 2 of complex $\mathbf{3}^{+}$.

Transitions	% contributions
HOMO-20 -> LUMO	6.515144
HOMO-12 -> LUMO	21.60247
HOMO-11 -> LUMO	6.860259
HOMO-7 -> LUMO	17.32073
HOMO-3 -> LUMO	7.461315
HOMO-2 -> LUMO	7.220255
HOMO-1 -> LUMO	9.656316
HOMO -> LUMO	23.36351

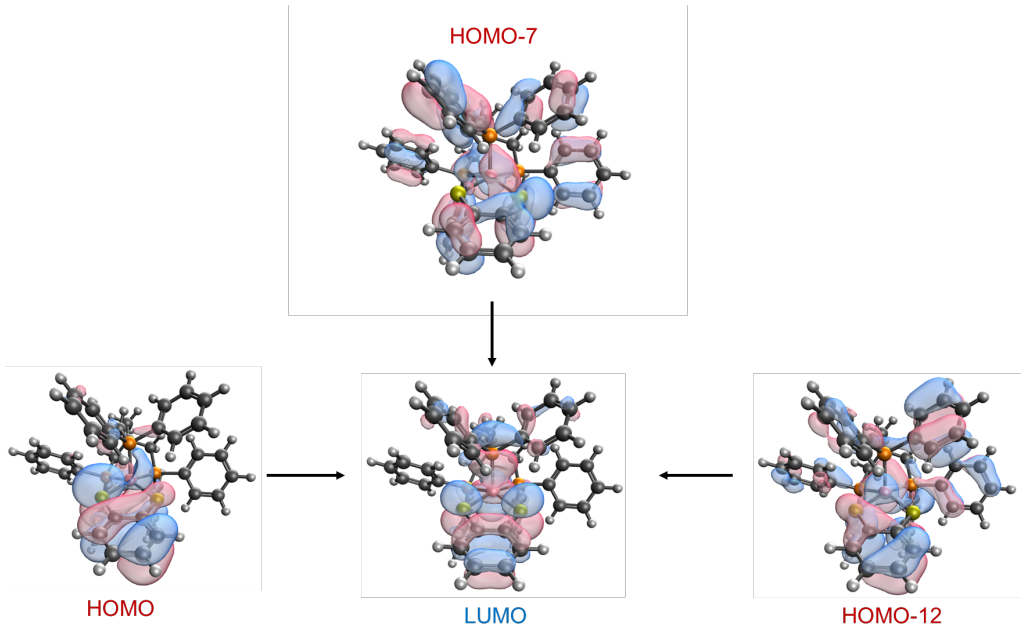

Figure S53. Origin of orbitals that highly contribute toward transition of excited state 2 of complex $\mathbf{3}^{+}$.

Table S5. Calculated relative contribution of transitions to excited state 1 of complex $\mathbf{3}^{+}$.

Transitions	% contributions
HOMO-19->LUMO	5.84626
HOMO-7->LUMO	8.469689
HOMO-5->LUMO	7.233084
HOMO-2->LUMO	10.46369
HOMO-1->LUMO	31.40727
HOMO->LUMO	36.5800

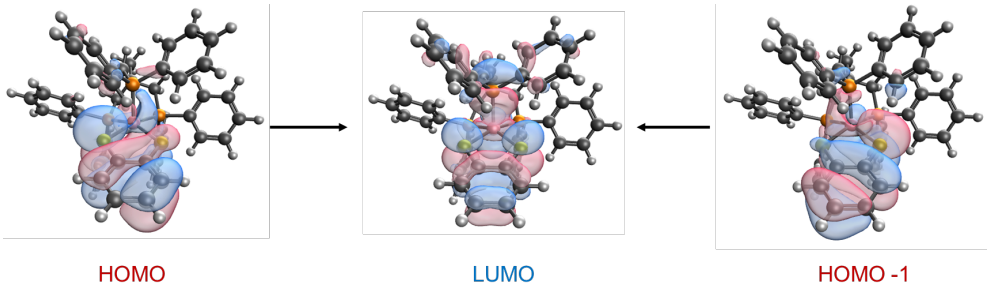

Figure S54. Origin of orbitals that highly contribute toward transition of excited state 1 of complex $\mathbf{3}^{+}$.

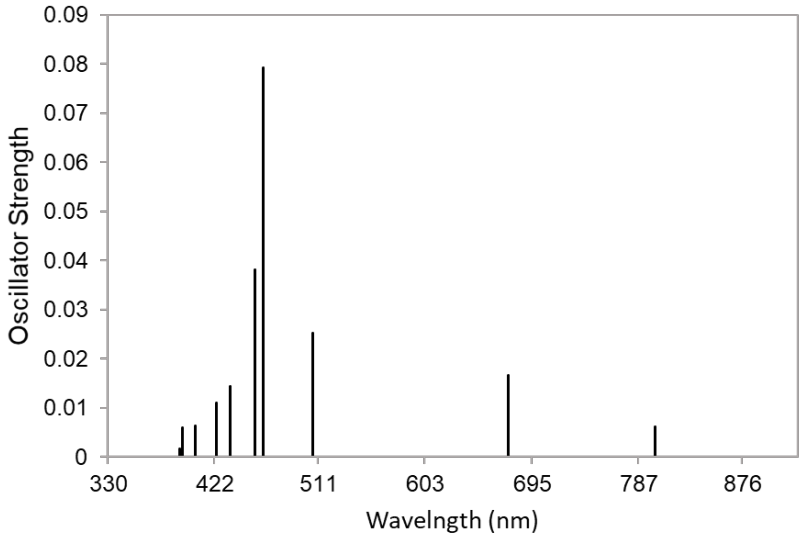

Figure S55. Calculated UV/Vis transitions and associated oscillator strengths for complex $\mathbf{3}^{+}$.

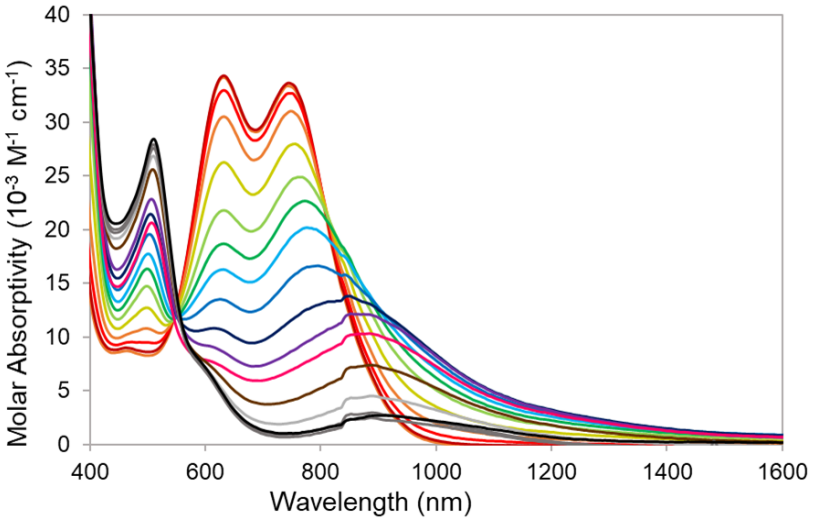

Figure S56. Vis-NIR spectral changes of **1** in a DCM solution of 0.25M [*n*Bu$_4$N][PF$_6$] under an atmosphere of N_2 as potential is cathodically shifted by 25 mV increments.

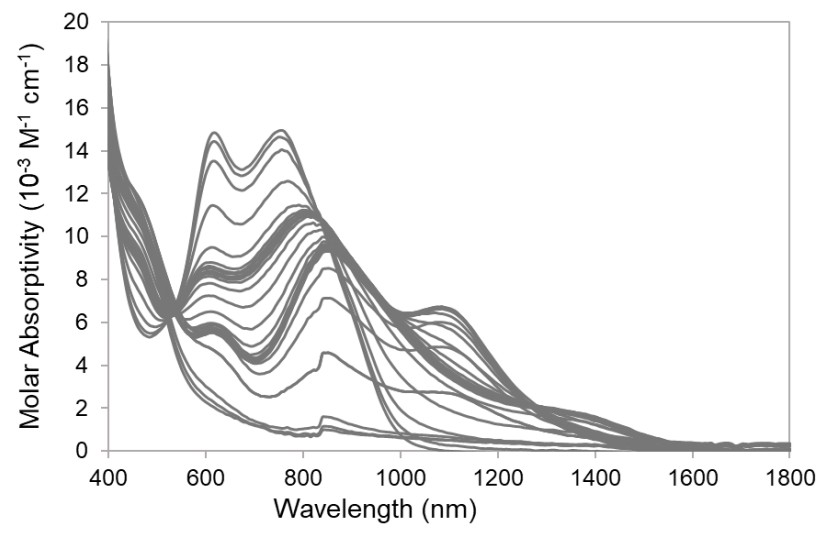

Figure S57. Vis-NIR spectral changes of **2** in a DCM solution of 0.25 M [*n*Bu$_4$N][PF$_6$] under an atmosphere of N_2 as potential is cathodically shifted by 25 mV increments.

Table S6. X-ray crystallography data and structure refinement for $\mathbf{1}^{3+}$.

Chemical formula	$C_{157}H_{157}B_3Co_3F_{12}N_3O_{2.50}P_9S_6$	
Formula weight	3034.16 g/mol	
Temperature	100(2) K	
Wavelength	0.71073 Å	
Crystal size	0.095 × 0.104 × 0.480 mm	
Crystal habit	black rod	
Crystal system	triclinic	
Space group	$P\bar{1}$	
Unit cell dimensions	a = 20.285(3) Å	α = 62.702(4)°
	b = 21.478(3) Å	β = 87.142(5)°
	c = 21.698(3) Å	γ = 71.516(5)°
Volume	7915.9(19) Å^3	
Z	2	
Density (calculated)	1.273 g/cm^3	
Absorption coefficient	0.546 mm^{-1}	
F(000)	3150	
Diffractometer	Bruker APEX DUO	
Radiation source	fine-focus tube (MoKα , λ = 0.71073 Å)	
Theta range for data collection	1.06 to 23.26°	
Index ranges	$-22 \le h \le 22$, $-23 \le k \le 23$, $-24 \le l \le 24$	
Reflections collected	133552	
Independent reflections	22693 [R(int) = 0.0901]	
Coverage of independent reflections	99.8%	
Absorption correction	multi-scan	
Max. and min. transmission	0.9500 and 0.7800	
Structure solution technique	direct methods	
Structure solution program	SHELXT 2014/5 (Sheldrick, 2014)	
Refinement method	Full-matrix least-squares on F^2	

Refinement program	SHELXL-2017/1 (Sheldrick, 2017)	
Function minimized	$\Sigma\, w(F_o^2 - F_c^2)^2$	
Data / restraints / parameters	22693 / 10 / 1718	
Goodness-of-fit on F^2	1.073	
Final R indices	15806 data; $I > 2\sigma(I)$	$R_1 = 0.0886$, $wR_2 = 0.2317$
	all data	$R_1 = 0.1277$, $wR_2 = 0.2573$
Weighting scheme	$w = 1/[\sigma^2(F_o^2) + (0.0694P)^2 + 113.0602P]$ where $P = (F_o^2 + 2F_c^2)/3$	
Largest diff. peak and hole	1.419 and –1.001 eÅ^{-3}	
R.M.S. deviation from mean	0.127 eÅ^{-3}	

Table S7. Average selected bond angles (°) for complex $\mathbf{1}^{3+}$.

S–Co–S	89.78(6)
S–Co–P_{apical}	107.02(77)
S–Co–P_{basal}	87.14(7)
P_{apical}–Co–P_{basal}	92.71(4)

References:

(1) Sakamoto, R.; Kambe, T.; Tsukada, S.; Takada, K.; Hoshiko, K.; Kitagawa, Y.; Okumura, M.; Nishihara, H. Π-Conjugated Trinuclear Group-9 Metalladithiolenes With a Triphenylene Backbone. *Inorg. Chem.* **2013**, *52* (13), 7411–7416. https://doi.org/10.1021/ic400110z.

(2) Harnisch, J. A.; Angelici, R. J. Gold and Platinum Benzenehexathiolate Complexes as Large Templates for the Synthesis of 12-Coordinate Polyphosphine Macrocycles. *Inorganica Chim. Acta* **2000**, *300–302*, 273–279. https://doi.org/10.1016/S0020-1693(99)00552-6.

(3) Claramunt, R. M.; Elguero, J. Proton, Carbon-13, and Fluorine-19 NMR Study of N-Arylpyridinium Salts: Attempted Calculations of the Σ1 and ΣR0 Values for N-Pyridinium Substituents. *Collect. Czechoslov. Chem. Commun.* **1981**, *46* (3), 584–596.

https://doi.org/10.1135/cccc19810584.

(4) Addison, A. W.; Rao, T. N.; Reedijk, J.; van Rijn, J.; Verschoor, G. C. Synthesis, Structure, and Spectroscopic Properties of Copper(II) Compounds Containing Nitrogen–Sulphur Donor Ligands; the Crystal and Molecular Structure of Aqua[1,7-Bis(N-Methylbenzimidazol-2′-Yl)-2,6-Dithiaheptane]Copper(II) Perchlorate. *J. Chem. Soc., Dalt. Trans.* **1984**, No. 7, 1349–1356. https://doi.org/10.1039/DT9840001349.

(5) Krejčik, M.; Daněk, M.; Hartl, F. Simple Construction of an Infrared Optically Transparent Thin-Layer Electrochemical Cell. *J. Electroanal. Chem. Interfacial Electrochem.* **1991**, *317* (1–2), 179–187. https://doi.org/10.1016/0022-0728(91)85012-e.

(6) Brunschwig, B. S.; Creutz, C.; Sutin, N. Optical Transitions of Symmetrical Mixed-Valence Systems in the Class II-III Transition Regime. *Chem. Soc. Rev.* **2002**, *31* (3), 168–184. https://doi.org/10.1039/b008034i.

(7) Shao, Y.; Molnar, L. F.; Jung, Y.; Kussmann, J.; Ochsenfeld, C.; Brown, S. T.; Gilbert, A. T. B.; Slipchenko, L. V.; Levchenko, S. V.; O'Neill, D. P.; DiStasio Jr, R. A.; Lochan, R. C.; Wang, T.; Beran, G. J. O.; Besley, N. A.; Herbert, J. M.; Yeh Lin, C.; Van Voorhis, T.; Hung Chien, S.; Sodt, A.; Steele, R. P.; Rassolov, V. A.; Maslen, P. E.; Korambath, P. P.; Adamson, R. D.; Austin, B.; Baker, J.; Byrd, E. F. C.; Dachsel, H.; Doerksen, R. J.; Dreuw, A.; Dunietz, B. D.; Dutoi, A. D.; Furlani, T. R.; Gwaltney, S. R.; Heyden, A.; Hirata, S.; Hsu, C.-P.; Kedziora, G.; Khalliulin, R. Z.; Klunzinger, P.; Lee, A. M.; Lee, M. S.; Liang, W.; Lotan, I.; Nair, N.; Peters, B.; Proynov, E. I.; Pieniazek, P. A.; Min Rhee, Y.; Ritchie, J.; Rosta, E.; David Sherrill, C.; Simmonett, A. C.; Subotnik, J. E.; Lee Woodcock III, H.; Zhang, W.; Bell, A. T.; Chakraborty, A. K.; Chipman, D. M.; Keil, F. J.; Warshel, A.; Hehre, W. J.; Schaefer III, H. F.; Kong, J.; Krylov, A. I.; Gill, P. M. W.; Head-Gordon, M. Advances in Methods and Algorithms in a Modern Quantum Chemistry Program Package. *Phys. Chem. Chem. Phys.* **2006**, *8* (27), 3172–3191. https://doi.org/10.1039/B517914A.

(8) Ditchfield, R.; Hehre, W. J.; Pople, J. A. Self-Consistent Molecular-Orbital Methods. IX. An Extended Gaussian-Type Basis for Molecular-Orbital Studies of Organic Molecules. *J. Chem. Phys.* **1971**, *54* (2), 724–728. https://doi.org/10.1063/1.1674902.

(9) Perdew, J. P.; Burke, K.; Ernzerhof, M. Generalized Gradient Approximation Made Simple. *Phys. Rev. Lett.* **1996**, *77* (18), 3865–3868. https://doi.org/10.1103/PhysRevLett.77.3865.

(10) Hehre, W. J.; Ditchfield, R.; Pople, J. A. Self — Consistent Molecular Orbital Methods . XII . Further Extensions of Gaussian — Type Basis Sets for Use in Molecular Orbital Studies of Organic Molecules Published by the AIP Publishing Articles You May Be Interested in Selfconsistent Molecular Orbit. *J. Chem. Phys.* **1972**, *56* (1985), 2257–2261.

(11) Orchanian, N. M.; Hong, L. E.; Velazquez, D. A.; Marinescu, S. C. Electrocatalytic Syngas Generation with a Redox Non-Innocent Cobalt 2-Phosphinobenzenethiolate Complex. *Dalt. Trans.* **2021**, *50*, 10779–10788. https://doi.org/10.1039/D0DT03270K.

(12) Cossi, M.; Rega, N.; Scalmani, G.; Barone, V. Energies, Structures, and Electronic Properties of Molecules in Solution with the C-PCM Solvation Model. *J. Comput. Chem.*

2003, *24* (6), 669–681. https://doi.org/10.1002/jcc.10189.

(13) Becke, A. D. Density-Functional Thermochemistry. III. The Role of Exact Exchange. *J. Chem. Phys.* **1993**, *98* (7), 5648–5652. https://doi.org/10.1063/1.464913.

(14) Wohlfarth, C. W. Permittivity (Dielectric Constant) of Liquids. In *CRC Handbook of Chemistry and Physics*; Rumble, J., Ed.; CRC Press, 2021; pp 6-187-6–208.

(15) Rappe, A. K.; Casewit, C. J.; Colwell, K. S.; Goddard, W. A.; Skiff, W. M. UFF, a Full Periodic Table Force Field for Molecular Mechanics and Molecular Dynamics Simulations. *J. Am. Chem. Soc.* **1992**, *114* (25), 10024–10035. https://doi.org/10.1021/ja00051a040.

(16) Ghilardi, C. A.; Laschi, F.; Midollini, S.; Orlandini, A.; Scapacci, G.; Zanello, P. Synthesis, Crystal Structure, Electrochemistry and Electronic Paramagnetic Resonance Spectroscopy of [M{(PPh2CH2)3CMe}(o-S2C6H4)][PF6] n (M = Fe, Co or Rh; N= 0 or 1). *J. Chem. Soc. Dalt. Trans.* **1995**, *1* (4), 531. https://doi.org/10.1039/dt9950000531.